

ESD-TR-67-562
ESTI FILE COPY

ESD RECORD COPY

RETURN TO
SCIENTIFIC & TECHNICAL INFORMATION DIVISION
(ESTI), BUILDING 1211

ESD ACCESSION LIST

ESTI Call No. 59411

Copy No. 1 of 1 CS

4

Solid State Research

1967

Prepared under Electronic Systems Division Contract AF 19(628)-5167 by

Lincoln Laboratory

MASSACHUSETTS INSTITUTE OF TECHNOLOGY

Lexington, Massachusetts



ADD 66654205

The work reported in this document was performed at Lincoln Laboratory, a center for research operated by Massachusetts Institute of Technology, with the support of the U.S. Air Force under Contract AF 19(628)-5167.

This report may be reproduced to satisfy needs of U.S. Government agencies.

This document has been approved for public release and sale; its distribution is unlimited.

Non-Lincoln Recipients

PLEASE DO NOT RETURN

Permission is given to destroy this document when it is no longer needed.

4

Solid State Research

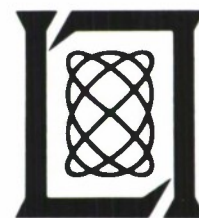
1967

Issued 31 January 1968

Lincoln Laboratory

MASSACHUSETTS INSTITUTE OF TECHNOLOGY

Lexington, Massachusetts



ABSTRACT

This report covers in detail the solid state research work at Lincoln Laboratory for the period 1 August through 31 October 1967. The topics covered are Solid State Device Research, Optical Techniques and Devices, Materials Research, and Physics of Solids.

Accepted for the Air Force
Franklin C. Hudson
Chief, Lincoln Laboratory Office

INTRODUCTION

I. SOLID STATE DEVICE RESEARCH

Photovoltaic detectors with high quantum efficiencies and high detectivities at 12°K have been fabricated from Bridgman-grown and subsequently annealed $\text{Pb}_{0.8}\text{Sn}_{0.2}\text{Te}$ crystals. The p-n junctions were prepared by diffusing approximately 15- μ deep n-type layers into p-type substrates with carrier concentrations ranging from 2 to $7 \times 10^{17} \text{ cm}^{-3}$. The cutoff wavelength of these detectors is 13 and 17 μ at 77° and 12°K, respectively. At 12°K, the quantum efficiency is about 40 percent, and the detectivity is between 2 and $4 \times 10^{10} \text{ cm/Wsec}^{1/2}$. Since about half the incident radiation is reflected at the surface, the measured quantum efficiency corresponds to an internal collection efficiency of about 80 percent.

Measurements of the noise voltages of photovoltaic $\text{Pb}_{1-x}\text{Sn}_x\text{Te}$ and $\text{Pb}_{1-y}\text{Sn}_y\text{Se}$ detectors have shown that at frequencies in the 1-kHz range the noise is dominated by the Johnson noise of the incremental diode resistance at zero bias, which for state-of-the-art diodes operated at 77°K ranges from 1 to 10 ohms. To achieve background-limited operation at 12 μ in a detector of unit quantum efficiency at 77°K, a resistance of 20 ohms is required for a 1-nm² diode. In the present diodes, the resistance at zero bias is determined by bulk leakage, possibly due to metallic inclusions in the crystal. Such metallic inclusions and low-angle grain boundaries have been revealed in some Bridgman-grown crystals of $\text{Pb}_{1-x}\text{Sn}_x\text{Te}$ by electrolytic etching.

Infrared images in the 4- to 5- μ range have been detected using the radiation-sensitive characteristics of a uniform InSb metal-oxide-semiconductor structure. The infrared images are detected by rapidly scanning the device with 0.63- μ light from a CW He-Ne laser. The detection depends on the highly nonlinear photoresponse of the structure, whereby the presence of the 4- to 5- μ image affects the signal generated by the 0.63- μ light. In addition, optical information at 1 μ has been read in and stored for over 1 hour using this same InSb-MOS structure. The information can be nondestructively read out using 5- μ radiation and can be erased with 0.25- μ radiation. This operation depends on the difference between the effect of 1- and 0.25- μ radiation on the population of electron states in the oxide or at the semiconductor-oxide interface. The local population then affects the response of the device to the 5- μ radiation.

Several major equipment modifications have been made in the 400-keV Van de Graaff accelerator system used to implant heavy ions in semiconducting crystals. These modifications have been primarily in the vacuum system and in the ion source. Following these alterations, the modified system has operated reliably delivering over 1 μA of As^+ ions at drift tube and sample chamber pressures of 10^{-6} torr or less.

This system has been used to implant p-type germanium samples with As^+ and N^+ ions. For the As^+ implants, doses ranged from 2×10^{12} to 1.6×10^{16} ions/cm², and the target temperature was varied between 20° and 500°C. The room-temperature implants required post implantation annealing to over 400°C to produce conversion to n-type. However, most of the implants performed with the germanium wafers elevated to temperatures in the 450° to 500°C range produced n-type conductivity immediately. To date, the results obtained with N^+ are inconclusive.

CdTe has been bombarded with 400-keV N^+ and As^+ ions which should be p-type dopants. To date, the N^+ implantation has given no indication of converting CdTe; however, the As^+ implants have shown some promising results. Materials problems, however, have hampered the reproducibility of these results. An annealing program has been initiated to achieve homogeneous starting material.

II. OPTICAL TECHNIQUES AND DEVICES

Short-term stability measurements have been made on improved versions of the CO_2 - N_2 -He lasers previously described. For an observation time of 0.1 sec, the frequency is stable to less than 400 Hz. An order of magnitude improvement is expected upon elimination of power ripple and coolant temperature variations.

A sealed-off CO_2 laser has been operated for over 1000 hours. Analysis of the gas content at this time indicates that the heated nickel cathode maintains the proper CO_2 concentration, thus circumventing the usual CO_2 loss observed to degrade performance in previous experiments.

A 9-meter long CO_2 amplifier is under construction. Preliminary tests of the first 3-meter section indicate that the final system should yield at least 100-W continuous output.

III. MATERIALS RESEARCH

The eutectic phase diagram of the PbSe-SnSe pseudo-binary system has been determined by differential thermal analysis. At the eutectic temperature (870°C), the solubility of SnSe in PbSe (rocksalt structure) is 52 mole-percent, and the solubility of PbSe in SnSe (orthorhombic structure) is 24 mole-percent.

The results of magnetic susceptibility measurements have confirmed an earlier report that SrRuO_3 is ferromagnetic and that CaRuO_3 has antiferromagnetic interactions. These measurements show that CaRuO_3 has a Néel temperature of $110^\circ \pm 10^\circ \text{K}$, and exhibits a small parasitic ferromagnetism below 77°K. Data on neutron diffraction and on magnetization at fields up to 125 kOe show that SrRuO_3 exhibits collective-electron magnetism and that both the spin-up and spin-down bands contain holes. The presence of holes in both bands presumably accounts for the fact that the interactions in this compound are ferromagnetic rather than antiferromagnetic.

Introduction

The pressure coefficient of the Curie temperature, dT_c/dP , was found to be negative for the magnetic spinels CdCr_2Se_4 , CuCr_2Se_4 , and CuCr_2S_4 . For CdCr_2Se_4 , this indicates that a reduction in lattice size increases the antiferromagnetic direct superexchange interaction between B-sites more rapidly than the ferromagnetic 90° superexchange interaction between these sites. It is probable that the same mechanism is primarily responsible for the negative pressure coefficients of the Cu spinels, but the band electrons in these compounds could also be contributing to the negative coefficient.

Theoretical relationships between various electronic phases, including ferromagnetic, antiferromagnetic, metamagnetic, and Pauli paramagnetic, have been summarized by constructing a qualitative electronic phase diagram. The diagram gives the boundaries between the phases in terms of the parameters n_d , the number of electrons per relevant orbital, and the energy transfer integral b which appears in tight-binding collective-electron theory and in localized-electron superexchange theory.

IV. PHYSICS OF SOLIDS

The mechanically integrated thin-film package, previously developed for electroreflectance studies, has now been adapted to electroabsorption. The new technique allows the simultaneous measurement of both these effects and a comparison by means of the Kramers-Kronig transforms.

Recently, it has been suggested that the plateau in the temperature variation of the conductivity of HgTe , which is observed in pure samples in the vicinity of 20° to 30°K , arises from an excitonic insulator to a semimetal transition. Our measurements indicate that this plateau can be attributed to a reasonable variation of carrier concentration and mobility with temperature.

A system for automatically recording and processing spectrometer data has been devised, built, and placed into operation. The system has been applied to the study of the effects of a uniaxial stress on the impurity spectrum of phosphorous-doped silicon. The pure shear deformation potential, $E_2 = 7.9 \pm 0.2\text{eV}$, measured here agrees with the value previously obtained in sulfur-doped silicon.

By use of the exciton theory, which has been previously confirmed by experiment, the motion of the Landau levels in the interband magnetoabsorption of InSb has been obtained. The conduction band Landau levels move as expected from the Bowers-Yafet theory, whereas valence band levels do not, probably because the top of the valence band is not at $\vec{k} = 0$.

A variational trial function has been developed for the polaron problem which gives the exact ground state energy through order α^2 at weak coupling and, with computer calculations, "variational" effective masses which are expected to be highly accurate for $\alpha \lesssim 4$.

The upper limit on the number of bound states of a particle in a semidefinite nonlocal potential has been derived by a generalization of a procedure used by Schwinger for a local potential. Applications for specific potential expressions have been worked out.

The magneto-elastic coupling of magnetic and elastic waves in magnetic metallic films has been studied directly for the first time by means of spin wave resonance in the vicinity of 60GHz. By curve fitting in the crossover region, the magneto-elastic coupling constant, speed of transverse microwave phonons in the film, and phonon relaxation time were determined.

Microwave resonance results on CoCr_2O_4 as a function of temperature are being analyzed on the basis of a modification of the molecular field model of Dwight and Menyuk. The two resonances observed at temperatures above the spiral spin ordering temperature (31°K) are associated with a high-frequency exchange mode and a low-frequency uniform mode; the interpretation of the two resonance modes below 31°K is awaiting the results of molecular field calculations which are presently under way.

A study of the effects of pressure, up to 5kbars, on the magnetic properties of MnAs has been initiated. The phase diagram in the region between 70° and 320°K has been mapped out by measuring directly the magnetic moment as a function of pressure.

The Heisenberg model susceptibility has been expanded in terms of the Langevin parameter $u \equiv \mathcal{L}(2J/kT)$ and a formal similarity with the $S = 1/2$ Ising model has been noted. The new expansion permits more reliable extrapolations for one-, two-, and three-dimensional lattices. Critical properties have also been calculated in terms of high-temperature expansions for the Vaks-Larkin model, which is essentially equivalent to a lattice of isotropically interacting two-dimensional unit vectors (or classical spins). The properties which have been studied so far, namely T_c , γ , and α , appear to be bounded on one side by those predicted from the one-dimensional Ising model, and on the other side by those of the three-dimensional Heisenberg model.

A study has been carried out of spontaneous and stimulated Raman emission from the lowest optical E-vibration in α -quartz. The relaxation rate, as determined from the linewidth, is very high, ~ 20 to 100 times faster than the generation rate as measured by Stokes production. Furthermore, the phonon reabsorption rate as determined from anti-Stokes generation is comparable to pure phonon emission near the phase-matched angle. These factors make the observation of far infrared radiation during the stimulated Raman process difficult.

It has been found that when a mode-locked, Q-switched ruby laser is pumped hard enough to double pulse, the second pulse contains more regular and probably higher power spikes than the first. It is suggested that this is the cause of the high breakage rate of ruby rods in rotating prism Q-switched lasers in the double Brewster configuration.

An experimental investigation of thermal self-defocusing arising from the passage of a laser beam in an absorbing liquid cell has been initiated. The time dependence of the process is being studied quantitatively.

The possibility of maser emission from excited OH Λ -doublet states has been investigated. Trapped infrared resonance radiation, generated in the cascades following ultraviolet or chemical pumping to higher excited states, might invert the $\pi_{1/2}$ and anti-invert the $\pi_{5/2}$ Λ -doublets, resulting in observable signals if an early-type star were a fraction of a light year away from the OH.

CONTENTS

Abstract	iii
Introduction	iv
Organization	x
Reports by Authors Engaged in Solid State Research	xi
 I. SOLID STATE DEVICE RESEARCH	 1
A. High-Efficiency $\text{Pb}_{1-x}\text{Sn}_x\text{Te}$ Photovoltaic Detectors	1
B. Noise Measurements in Lead-Tin Chalcogenide Detectors	1
C. Metallic Inclusions and Low-Angle Grain Boundaries in $\text{Pb}_{1-x}\text{Sn}_x\text{Te}$ Crystals	5
D. Imaging and Storage with Uniform MOS Structure	5
E. Ion Implantation	8
1. Equipment Modifications	8
2. Ion Implantation of Germanium	8
3. Ion Implantation of CdTe	9
 II. OPTICAL TECHNIQUES AND DEVICES	 11
A. Stability Measurements of $\text{CO}_2\text{-N}_2\text{-He}$ Lasers at 10.6- μm Wavelength	11
B. Continuous Operation of a Sealed-Off CO_2 Laser Tube	13
C. 100-W CO_2 Amplifier at 10.6 μm	14
 III. MATERIALS RESEARCH	 15
A. PbSe-SnSe Pseudo-Binary System	15
B. Magnetic Properties of SrRuO_3 and CaRuO_3	15
C. Pressure Dependence of Magnetic Transitions in Spinels	19
D. Construction of an Electronic Phase Diagram	19
 IV. PHYSICS OF SOLIDS	 25
A. Electronic Band Structure	25
1. Electroabsorption in Bulk Single Crystals of Germanium	25
2. Unusual Temperature Dependence of Conductivity in HgTe	29
3. Effects of Calibrated Uniaxial Stress on Impurity Spectrum of Phosphorous-Doped Silicon	31
4. Automatic Recording of Spectrometer Data	31
5. Analysis of Landau Levels in InSb	33
6. Polaron Ground State Energy	35
7. Upper Bounds on Number of Bound States for Nonlocal Potential	36

B. Magnetism	37
1. Observation of Magneto-Elastic Coupling in Metallic Films	37
2. Magnetic Resonance in Spinel Compound CoCr_2O_4	39
3. Magnetic Properties of MnAs	39
4. New Expansion for Classical Heisenberg Model and Its Similarity to $S = 1/2$ Ising Model	41
5. Critical Properties of Vaks-Larkin Model for λ Transition in a Bose Fluid	42
C. Laser Scattering Experiments and Nonlinear Effects	45
1. Raman Scattering from Lowest Optical E-Vibration in α -Quartz	45
2. Mode Locking in Q-Switched Ruby Laser	47
3. Thermal Defocusing of Light in Liquids	48
4. Infrared Radiation Effects on OH Maser Emission	49

ORGANIZATION

SOLID STATE DIVISION

A. L. McWhorter, *Head*
 P. E. Tannenwald, *Associate Head*
 M. J. Hudson, *Assistant*
 E. P. Warekois

SOLID STATE THEORY

H. J. Zeiger, *Leader*
 M. M. Litvak, *Assistant Leader*

Argyres, P. N.	Kelley, P. L.
Chinn, S. R.*	Kleiner, W. H.
Dresselhaus, G. F.	Landon, S. N.
Hamilton, D. C.	Larsen, D. M.
Hanus, J. G. C.	Palm, B. J.†
Hartung, W. G.	Sigel, J. L.*
Kaplan, T. A.	Stanley, H. E.

OPTICS AND INFRARED

R. H. Kingston, *Leader*
 R. J. Keyes, *Assistant Leader*

Bates, D. H.	McPhie, J. M.
Bostick, H. A.	Quist, T. M.
Carbone, R. J.	Ross, A. H. M.
Freed, C.	Sullivan, F. M.
Hinkley, E. D.	Zimmerman, M. D.
Longaker, P. R.	

ELECTRONIC MATERIALS

J. B. Goodenough, *Leader*
 A. J. Strauss, *Associate Leader*

Anderson, C. H., Jr.	LaFleur, W. J.
Andrews, H. I.*	Lavine, M. C.†
Arnott, R. J.	Longo, J. M.
Banus, M. D.	Mastromattei, E. L.
Batson, D. A.	O'Connor, J. R.
Brebrick, R. F., Jr.	Owens, E. B.
Button, M. J.	Plonko, M. C.
Delaney, E. J.	Pollard, E. R.*
England, R. E.	Raccach, P. M.
Fahey, R. E.	Reed, T. B.
Ferretti, A.	Roddy, J. T.
Finn, M. C.	Searles, I. H.
Hilsenrath, S.	Smith, F. T. J.
Iseler, G. W.	Steininger, J. M.
Kafalas, J. A.	Wheatley, G. E.
Kasper, H.	

SOLID STATE PHYSICS

J. G. Mavroides, *Leader*
 G. B. Wright, *Assistant Leader*

Brandt, R. C.	Krag, W. E.
Burke, J. W.	Melngailis, J.
Carman, R. L.	Menyuk, N.
Dickey, D. H.	Murphy, H. C.
Dresselhaus, M. S.‡	NiH, K. W.
Dwight, K., Jr.	Parker, C. D.
Feinleib, J.	Perry, F. H.
Feldman, B.	Pine, A. S.
Fulton, M. J.	Scouler, W. J.
Groves, S. H.	Stickler, J. J.*
Henrich, V. E.	Strahm, N. D.*
Johnson, E. J.	Thaxter, J. B.
Kernan, W. C.	Tichovolsky, E. J.*
Kolesar, D. F.	Weber, R.

APPLIED PHYSICS

J. O. Dimmock, *Leader*
 T. C. Harman, *Assistant Leader*
 I. Melngailis, *Assistant Leader*

Butler, J. F.	Finne, P. C.	Oliver, M. R.*
Calawa, A. R.	Foyt, A. G.	Paladino, A. E.
Carter, F. B.	Hurwitz, C. E.	Phelan, R. J., Jr.
Caswell, F. H.	Lindley, W. T.	Stillman, G. E.
Clough, T. F.	Matthews, W.*	Ward, J. H. R., III
Donaldson, P. L.	Mooradian, A.	Wolfe, C. M.
Donnelly, J. P.	Murphy, R. A.*	Youtz, P.

* Research Assistant

† Part Time

‡ Leave of Absence

REPORTS BY AUTHORS ENGAGED IN SOLID STATE RESEARCH

15 August through 15 November 1967

PUBLISHED REPORTS

Technical Report

TR No.				<u>DDC and Hayden Nos.</u>
435	LCAO Secular Determinant Program	D. Esterling	12 July 1967	DDC 659749

Journal Articles*

JA No.			
2805	Spin Waves in Paramagnetic Fermi Gases	L. L. VanZandt	Phys. Rev. <u>162</u> , 399 (1967)
2939	Fourier Expansion for the Electronic Energy Bands in Silicon and Germanium	G. F. Dresselhaus M. S. Dresselhaus	Phys. Rev. <u>160</u> , 649 (1967), DDC 662302
2964	Temperature Dependence, Orientation Correlation, and Molecular Fields in Second-Harmonic Light Scattering from Liquids and Gases	D. L. Weinberg	J. Chem. Phys. <u>47</u> , 1307 (1967)
2973	The Crystal Structure of Neodymium Monotelluroxide-Nd ₂ O ₂ Te	P. M. Raccach J. M. Longo H. A. Eick†	Inorg. Chem. <u>6</u> , 1471 (1967), DDC 658765
2977	Interband Magnetoreflexion and Band Structure of HgTe	S. H. Groves R. N. Brown† C. R. Pidgeon†	Phys. Rev. <u>161</u> , 779 (1967)
2989	A Thermodynamic Investigation of the Compounds In ₃ SbTe ₂ , InSb and InTe	A. K. Jena† M. B. Bever† M. D. Banus	Trans. Met. Soc. AIME <u>239</u> , 1232 (1967)
2998	Hall Coefficient and Transverse Magnetoresistance in HgTe at 4.2°K and 77°K	T. C. Harman J. M. Honig P. H. Trent	J. Phys. Chem. Solids <u>28</u> , 1995 (1967)
3025	InSb-GaAsP Infrared to Visible Light Converter	R. J. Phelan, Jr.	Proc. IEEE (Correspondence) <u>55</u> , 1501 (1967), DDC 662175

* Reprints available.

† Author not at Lincoln Laboratory.

Reports

JA No.

3060	Polarization and Intensity of Raman Scattering from Plasmons and Phonons in Gallium Arsenide	A. Mooradian A. L. McWhorter	Phys. Rev. Letters <u>19</u> , 849 (1967)
3070	Tetrahedral-Site Copper in Chalcogenide Spinels	J.B. Goodenough	Solid State Commun. <u>5</u> , 577 (1967)
3080	Current Runaway and Avalanche Effects in n-CdTe	M.R. Oliver A. L. McWhorter A.G. Foyt	Appl. Phys. Letters <u>11</u> , 111 (1967), DDC 662292
3085	Observation of Exciton Fine Structure in the Interband Magnetoabsorption of InSb and Germanium	E.J. Johnson	Phys. Rev. Letters <u>19</u> , 352 (1967), DDC 662293
3087	Inversion Asymmetry Effects on Oscillatory Magnetoresistance in HgSe	L.M. Roth* S.H. Groves P.W. Wyatt*	Phys. Rev. Letters <u>19</u> , 576 (1967)
3091	Electroreflectance Study of Interband Magneto-Optical Transitions in InAs and InSb at 1.5°K	C.R. Pidgeon* S.H. Groves J. Feinleib	Solid State Commun. <u>5</u> , 677 (1967)
3126	Electron-Hole Pair Effects on Landau Levels of InSb	D.M. Larsen	Phys. Rev. Letters <u>19</u> , 1128 (1967)

UNPUBLISHED REPORTS

Journal Articles

JA No.

3038	Long-Term Operation of a Sealed CO ₂ Laser	R.J. Carbone	Accepted by IEEE J. Quant. Electron.
3044	Optical Properties of the Metal ReO ₃ from 0.1 to 22 eV	J. Feinleib W.J. Scouler A. Ferretti	Accepted by Phys. Rev.
3049	Characterization and Structure of La ₄ Re ₆ O ₁₉ : A New Metal Cluster Compound	J.M. Longo A.W. Sleight*	Accepted by Inorg. Chem.
3065	Self-Steepening of Light Pulses	F. De Martini* C.H. Townes* T.K. Gustafson* P.L. Kelley	Accepted by Phys. Rev.

* Author not at Lincoln Laboratory.

JA No.

3078	Infrared Heterodyne Detection	M. C. Teich	Accepted by Proc. IEEE
3104	Shallow Donors of InSb in a Magnetic Field	D. M. Larsen	Accepted by J. Phys. Chem. Solids
3107	Mode Pulling in a Stimulated Raman Oscillator	P. E. Tannenwald	Accepted by J. Appl. Phys.
3108	Magnetic Properties of $\text{La}_{.5}\text{Sr}_{.5}\text{CoO}_3$ Near Its Curie Temperature	N. Menyuk P. M. Racciah K. Dwight	Accepted by Phys. Rev.
3110	A New, Widely and Continuously Tunable, High Power Pulsed Laser Source	R. L. Carman J. Hanus D. L. Weinberg	Accepted by Appl. Phys. Letters
3140	Crystal Growth, Annealing and Diffusion of Lead-Tin Chalcogenides	A. R. Calawa T. C. Harman M. C. Finn P. Youtz	Accepted by Trans. Met. Soc. AIME
3161	Growth of Single Crystals of ZnTe and $\text{ZnTe}_{1-x}\text{Se}_x$ by Temperature Gradient Solution Zoning	J. M. Steininger R. E. England	Accepted by Trans. Met. Soc. AIME
MS-2072	Metallurgical and Electronic Properties of $\text{Pb}_{1-x}\text{Sn}_x\text{Te}$, $\text{Pb}_{1-x}\text{Sn}_x\text{Se}$, and Other IV-VI Alloys	A. J. Strauss	Accepted by Trans. Met. Soc. AIME

Meeting Speeches*

MS No.

1742	Analysis of Tellurides of Lead and Tin by Automatic Titrations	J. C. Cornwell K. L. Cheng†	International Congress on Pure and Applied Chemistry, Prague, Czechoslovakia, 4 – 10 September 1967
1943	Analysis of Distant-Neighbor Interactions in Cubic Spinels	K. Dwight N. Menyuk	International Congress on Magnetism, Boston, Massachusetts, 10 – 16 September 1967
1945	NMR and Magnetization Studies of CdCr_2Se_4	G. H. Stauss† M. Rubinstein† J. Feinleib K. Dwight N. Menyuk A. Wold†	
1952	Observation of Magnetoelastic Coupling by Spin Wave Resonance	R. Weber	

* Titles of Meeting Speeches are listed for information only. No copies are available for distribution.

† Author not at Lincoln Laboratory.

Reports

MS No.

1954	Localized vs Collective Descriptions of Magnetic Electrons	J.B. Goodenough	} International Congress on Magnetism, Boston, Massachusetts, 10 – 16 September 1967
1955	Magnetic Properties of SrRuO_3 and CaRuO_3	J.M. Longo P.M. Racciah J.B. Goodenough	
1956	A Localized-Electron \leftrightarrow Collective-Electron Transition in the System $(\text{La}, \text{Sr})\text{CoO}_3$	P.M. Racciah J.B. Goodenough	
1958	Resistivity and Magnetic Order in Ti_2O_3	L.L. VanZandt J.M. Honig J.B. Goodenough	
1961	Observation of Ferri- and Antiferromagnetic Resonance in Insulating Magnetic Spiral Structures	J.J. Stickler H.J. Zeiger	
1959	Band Structure of Nickel and Low-Energy Optical Transitions	J. Hanus J. Feinleib W.J. Scouler	
1952B	An Analysis of Magnetoelastic Coupling in Magnetic Films	R. Weber	Seminar, Tufts University, 22 September 1967
1976B	The Evolution of Intense Short Pulses in Nonlinear Optical Media	P.L. Kelley F. De Martini* C.H. Townes* T.K. Gustafson*	} Third USSR Symposium on Non-linear Optics, Erevan, Armenia, U.S.S.R., 20 – 27 October 1967
2011	Stabilization of Trapped Beams	T.K. Gustafson* P.L. Kelley R.Y. Chiao*	
2012	Stimulated Light-by-Light Scattering	R.Y. Chiao* P.L. Kelley R.L. Carman E. Garmire*	
2018	Stimulated Raman Scattering in Quartz	P.E. Tannenwald	
1976C	The Evolution of Intense Short Pulses in Nonlinear Optical Media	P.L. Kelley F. De Martini* C.H. Townes* T.K. Gustafson*	Fall URSI Meeting, University of Michigan, 16 October 1967
1985	Crystal Growth, Annealing and Diffusion of Lead-Tin Chalcogenides	A.R. Calawa T.C. Harman M.C. Finn P. Youtz	AIIME, New York, 28 – 30 August 1967

* Author not at Lincoln Laboratory.

MS No.

1993	Growth of Single Crystals of ZnTe and $\text{ZnTe}_{1-x}\text{Se}_x$ by Temperature Gradient Solution Zoning	J.M. Steininger R.E. England	} Electronic Materials Conference, New York, 27 – 30 August 1967
2072	Metallurgical and Electronic Properties of $\text{Pb}_{1-x}\text{Sn}_x\text{Te}$, $\text{Pb}_{1-x}\text{Sn}_x\text{Se}$, and Other IV-VI Alloys	A.J. Strauss	
1996	High Power and Efficiency in CdS and CdSe Electron Beam Pumped Lasers	C.E. Hurwitz	} International Conference on II-VI Semiconducting Compounds, Brown University, 6 – 8 September 1967
2009	Homogeneity Range and Concentration-Pressure Isotherms of HgSe	R.F. Brebrick A.J. Strauss	
2013	Inversion Asymmetry Splittings from Oscillatory Magnetoresistance in HgSe	S.H. Groves L.M. Roth* P.W. Wyatt*	
2014	Low Temperature Reflection and Electroreflection Study of Interband Magneto-Optical Transitions in HgTe	C.R. Pidgeon* S.H. Groves	
2075	Band and Transport Parameters of Hg-Chalcogenides	T.C. Harman	
2079	Optical Absorption and Band Edge Parameters of Group II-VI Semiconductors	J.O. Dimmock	
2024	The Raman Spectrum of Trigonal, α -Monoclinic and Amorphous Selenium	A. Mooradian G.B. Wright	First International Symposium on Physics of Selenium and Tellurium, Montreal, Canada, 12 – 13 October 1967
2037	Structure of $\text{La}_4\text{Re}_6\text{O}_{19}$: A New Metal Cluster Compound	A.W. Sleight* J.M. Longo	American Crystallographic Association, Minneapolis, Minnesota, 20 – 25 August 1967
2049	$\text{Pb}_{1-x}\text{Sn}_x$ -Salt Infrared Diode Lasers	J.F. Butler	} NEREM, Boston, Massachusetts, 1 – 3 November 1967
2071	An Autotracking CO_2 Laser Radar	H.A. Bostick A.H.M. Ross	
2053	Influence of a New Chemical Bond on the Perovskite vs Defect-Pyrochlore Structures	P.M. Raccach J.M. Longo	Molecular Dynamics and Structure of Solids Conference, Gaithersburg, Maryland, 16 – 19 October 1967

* Author not at Lincoln Laboratory.

Reports

MS No.

2095	Recent Research on Spin Density	H.E. Stanley	Spin and Charge Density Conference, Sagamore, New York, 5 – 8 September 1967
2096	Spin Wave Resonance	R. Weber	International Colloquium on Magnetic Films, Boston, Massachusetts, 18 – 20 September 1967
2097	Etching of Silicon Nitride Using Thin Deposited Layers of Silicon as an Etch Mask	W.T. Lindley	Electrochemical Society, Chicago, Illinois, 15 – 20 October 1967
2100	The Effect of Pressure on Some Compound Semiconductors and Defect-Structure Metallic Oxides	M.D. Banus	Naval Research Laboratory, Washington, D.C., 9 October 1967
2112	Arc Techniques for Materials Preparation and Czochralski Crystal Growth	T.B. Reed	Conference on High Temperature Technology, Asilomar, California, 17 – 20 September 1967
2120	Raman Scattering Studies Using Laser Sources	A. Mooradian	Seminar, National Bureau of Standards, Washington, D.C., 26 October 1967
2121	Nonstoichiometry of Semiconducting Compounds	R.F. Brebrick	Materials Symposium, University of Missouri, 29 – 31 October 1967
2126	Laser Scanned Imaging and Storage Device	R.J. Phelan, Jr.	International Electron Devices Meeting, Washington, D.C., 18 – 20 October 1967
2132	A Phenomenological Theory for Dispersion Relations in Solids	G.F. Dresselhaus	Seminar, Harvard University, 25 October 1967
2149	Infrared Detection and Imaging Using an InSb-MOS Structure	J.O. Dimmock	Seminar, Yale University, 7 November 1967
2152, 2152A	Raman Scattering from Plasmons and Phonons in Semiconductors	A.L. McWhorter	Seminar, Purdue University, 10 November 1967; Seminar, Harvard University, 15 November 1967

I. SOLID STATE DEVICE RESEARCH

A. HIGH-EFFICIENCY $\text{Pb}_{1-x}\text{Sn}_x\text{Te}$ PHOTOVOLTAIC DETECTORS

Photovoltaic detectors with high quantum efficiencies and high detectivities at 12°K have been fabricated from Bridgman-grown and subsequently annealed $\text{Pb}_{0.8}\text{Sn}_{0.2}\text{Te}$ crystals. The p-n junctions were prepared by diffusing approximately 15- μ deep n-type layers into p-type substrates with carrier concentrations ranging from 2 to $7 \times 10^{17} \text{ cm}^{-3}$. Diffusion temperatures ranged from 400° to 450°C, and the times ranged from 40 to 150 hours. A crushed ingot of metal-rich $\text{Pb}_{0.8}\text{Sn}_{0.2}\text{Te}$ was used as a diffusion source. Photo-resist masking was used to define the 5-mil-diameter contact to the n-type layer, and the contacts were made by plating first a layer of gold and then a layer of indium.

The properties of two $\text{Pb}_{0.8}\text{Sn}_{0.2}\text{Te}$ detectors are given in Table I-1. The cutoff wavelengths of these detectors are 13 and 17 μ at 77° and 12°K, respectively. At 12°K the efficiency, defined as the number of carriers crossing the p-n junction per incident photon, is about 40 percent for both these detectors. Since about half the incident radiation is reflected at the surface, this corresponds to an internal collection efficiency of about 80 percent. The efficiency was measured by observing the change in the current of a reverse biased diode when the room-temperature background radiation falling on the detector was eliminated by placing a cooled object in front of the window. This gives the 300°K "black-body" efficiency up to the cutoff wavelength. Since these diodes have response spectra at 12°K which correspond closely to the spectrum of an ideal photon detector up to the cutoff wavelength, this efficiency corresponds closely to the efficiency computed from the peak responsivity, which was measured in the zero bias condition using a calibrated black-body source. The high efficiency is an indication that the surface recombination velocity is low and that the minority carrier diffusion length in the n-type layer is greater than the thickness of the layer.

At 77°K, the efficiency is greatly reduced. By studying the variation in sensitivity of the detectors as a function of position on the detector surface, we found that the response dropped off very rapidly with distance from the 5-mil-diameter contact; this was done by mechanically sweeping a focused helium-neon laser beam across the detector surface. This variation is due to the low junction resistance, which at 77°K becomes comparable to the radial resistance of the n-type layer. Since detector 73 has a smaller area than detector 555, we can expect the decrease in efficiency due to this effect to be smaller in detector 73. The efficiency values in Table I-1 are consistent with this expectation.

I. Melngailis T. C. Harman
A. R. Calawa W. T. Lindley
P. Youtz

B. NOISE MEASUREMENTS IN LEAD-TIN CHALCOGENIDE DETECTORS

Measurements of the noise voltages of photovoltaic $\text{Pb}_{1-x}\text{Sn}_x\text{Te}$ and $\text{Pb}_{1-y}\text{Sn}_y\text{Se}$ detectors at 77°K show that at frequencies in the 1-kHz range the noise is dominated by the Johnson noise of the incremental diode resistance.

TABLE I-1
PROPERTIES OF $\text{Pb}_{0.8}\text{Sn}_{0.2}\text{Te}$ PHOTOVOLTAIC DETECTORS

Detector	Hole Concentration in Substrate (cm^{-3})	Area (mm^2)	Temperature (°K)	Cutoff Wavelength (μ)	Zero Bias Incremental Resistance (ohms)	Efficiency (percent)	Peak Responsivity (V/W)	Peak Detectivity ($\text{cm/W sec}^{1/2}$)
73	2×10^{17}	0.45	12 77	17 13	6.8 1.8	40 7	40 1	2×10^{10} 8×10^8
555	6.6×10^{17}	1.7	12 77	17 13	18 1.3	40 1	110 0.15	4×10^{10} 3×10^8

TABLE I-2
PROPERTIES OF $\text{Pb}_{0.936}\text{Sn}_{0.064}\text{Se}$ PHOTOVOLTAIC DETECTORS AT 77°K

Detector	Area (mm^2)	Zero Bias Incremental Resistance (ohms)	Responsivity at 11μ (V/W)	Efficiency at 11μ	Measured Noise Voltage (V)	Calculated Noise Voltage (V)	Detectivity at 11μ ($\text{cm/W sec}^{1/2}$)
38	0.78	2.5	3.5	0.15	1.1×10^{-10}	1.0×10^{-10}	3×10^9
37	0.78	2.0	1.4	0.08	0.95×10^{-10}	0.92×10^{-10}	1.3×10^9
68	0.16	6.7	4.6	0.08	1.5×10^{-10}	1.7×10^{-10}	1.4×10^9

The incremental resistance of most state-of-the-art $\text{Pb}_{1-x}\text{Sn}_x\text{Te}$ and $\text{Pb}_{1-y}\text{Sn}_y\text{Se}$ detectors when operated at 77°K ranges from 1 to 10 ohms. In this impedance range, most preamplifiers have a noise figure which is too high for use in measuring the detector noise. We have used a Princeton Applied Research HR-8 lock-in amplifier as a simple voltmeter (without a reference signal) in conjunction with a type B preamplifier with an input step-up transformer ratio of 1:350. With this system, which has a rated noise figure of 1 dB in the vicinity of 1 kHz, for source impedances between 1 and 10 ohms, we were able to observe the noise from detectors with an impedance as low as 1.5 ohms at 77°K.

The measured detector noise voltage for an operating frequency of 900 Hz was, in all cases, in good agreement with the thermal noise voltage $V_n = (4kTR\Delta f)^{1/2}$ for the zero bias incremental diode resistance R at the operating temperature $T = 77^\circ\text{K}$ in a bandwidth $\Delta f = 1 \text{ Hz}$. As an additional test, a commercial resistor with the same resistance as the diode was substituted for the detector and cooled to 77°K. The noise voltage reading agreed well with the detector noise voltage. The detectivity of these detectors is thus limited by the expected thermal noise rather than by noise sources associated with contacts or surfaces, as has often been the case in polycrystalline film lead-salt detectors. Table I-2 shows values of measured and calculated noise voltage as well as the previously reported peak detectivity and external quantum efficiency of several $\text{Pb}_{1-y}\text{Sn}_y\text{Se}$ detectors at 77°K.

For a photovoltaic detector limited by thermal noise, the detectivity can be shown to be

$$D_\lambda^* = \frac{q\eta(R_A)^{1/2}}{2E_\lambda(kT)^{1/2}} \quad (1)$$

where η is the external quantum efficiency defined as the number of carriers reaching the p-n junction per incident photon, R_A is the incremental diode resistance of a unit area at zero bias in ohms-cm², E_λ is the energy per photon at the wavelength λ , and T is the operating temperature of the detector.

At a wavelength of 12 μ , the detectivity of a photovoltaic detector of unity quantum efficiency limited by the noise due to the photon flux of a room-temperature background for a 2π steradian aperture is about $5 \times 10^{10} \text{ cm/Wsec}^{1/2}$. From Eq.(1), we find that to achieve background-limited operation at this wavelength in a unity quantum-efficiency detector at 77°K, a diode resistance of about 0.2 ohm-cm² is required (20 ohms for a 1-mm² diode).

In the present diodes, the resistance at zero bias is determined by bulk leakage, possibly due to metallic inclusions in the crystal. In ideal diodes in which the current is due to minority carrier injection, the detectivity is limited by the reverse saturation current J_0 , since in such diodes $R_A = kT/qJ_0$. If, for example, the diode current is largely due to electrons, then $R_A \cong (kT\tau_e/q^3n_o^2\mu_e)^{1/2}$ where n_o is the equilibrium density of electrons in the p-region, μ_e is the electron mobility, and τ_e is the electron lifetime.

For an alloy whose energy gap at 77°K is 0.1 eV (peak photoresponse at about 12 μ), n_o is about 10^{10} cm^{-3} for a majority hole concentration of 10^{16} cm^{-3} . For a typical mobility of $2 \times 10^4 \text{ cm}^2/\text{V sec}$ and a lifetime of 10^{-8} sec , $R_A \cong 40 \text{ ohms-cm}^2$. This gives an estimate of $10^{12} \text{ cm/Wsec}^{1/2}$ for the maximum achievable detector-noise limited D_λ^* , if the quantum

Section I

-SS-6354

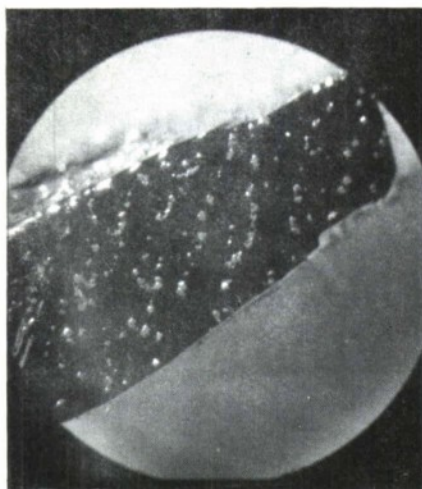


Fig. I-1. Etched sample from last-to-freeze end of $\text{Pb}_{1-x}\text{Sn}_x\text{Te}$ crystal A-2. Unannealed; linear magnification = 31.

-SS-6355

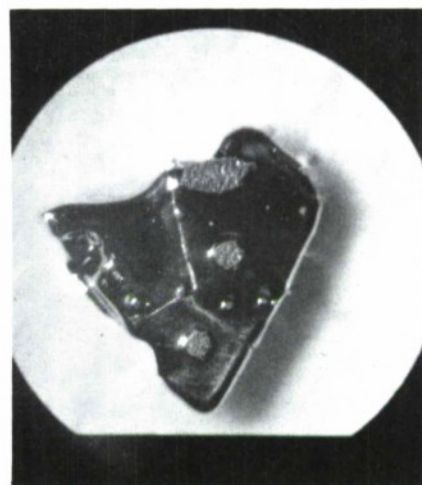


Fig. I-2. Etched sample from last-to-freeze end of $\text{Pb}_{1-x}\text{Sn}_x\text{Te}$ crystal A-2. After anneal; linear magnification = 31.

-SS-6356



Fig. I-3. Etched sample from first-to-freeze end of $\text{Pb}_{1-x}\text{Sn}_x\text{Te}$ crystal A-2. Unannealed; linear magnification = 100.

efficiency is assumed to be unity. For a diode in which hole injection predominates, the result would be nearly the same since the hole parameters in these materials are nearly the same as the electron parameters.

I. Melngailis

C. METALLIC INCLUSIONS AND LOW-ANGLE GRAIN BOUNDARIES IN $\text{Pb}_{1-x}\text{Sn}_x\text{Te}$ CRYSTALS

Electrolytic etching has revealed the existence of metallic inclusions and low-angle grain boundaries in some Bridgman-grown crystals of $\text{Pb}_{1-x}\text{Sn}_x\text{Te}$. The etching solution,¹ which consists of 20-g KOH, 45-ml H_2O , 35-ml glycerin, and 20-ml methanol, was used at room temperature and was stirred during the etching process. Current densities (with $\text{Pb}_{1-x}\text{Sn}_x\text{Te}$ samples at the anode) were about 0.5 A/cm^2 for showing the presence of metallic inclusions, and 0.05 A/cm^2 for revealing low-angle grain boundaries. The samples were rinsed in distilled water immediately after the etch.

$\text{Pb}_{1-x}\text{Sn}_x\text{Te}$ crystal A-2 was grown from a liquid with excess metal. The weighed-out proportions corresponded to the composition $(\text{Pb}_{0.70}\text{Sn}_{0.30})_{0.5063}\text{Te}_{0.4937}$. For the 400-g ingot, it was estimated that during crystal growth 7 mg of Te was present in the vapor space above the liquid. From electron microprobe and Hall coefficient measurements, the first-to-freeze solid composition was determined to be approximately $(\text{Pb}_{0.80}\text{Sn}_{0.20})_{0.499}\text{Te}_{0.501}$. $\text{Pb}_{1-x}\text{Sn}_x\text{Te}$ crystal A-4 was grown from an excess Te liquid in which the weighed-out proportions corresponded to $(\text{Pb}_{0.70}\text{Sn}_{0.30})_{0.49}\text{Te}_{0.51}$.

Figure 1-1 shows the surface of an etched sample of $\text{Pb}_{0.8}\text{Sn}_{0.2}\text{Te}$ crystal A-2 in which the inclusions are evident. The inclusions were only slightly affected by etching and remained as protuberances on the deeply etched semiconductor surface. This sample was obtained from the region near the last-to-freeze end of the crystal. Electron microprobe measurements showed that the inclusions were composed of a Pb-Sn alloy and, within the error of the measurements, contained no Te. Figure 1-2 shows an etched sample taken from the same region of crystal A-2 but which had been isothermally annealed at 850°C for seven days with a metal-rich powder of composition $(\text{Pb}_{0.8}\text{Sn}_{0.2})_{0.5125}\text{Te}_{0.4875}$. The annealing has decreased the density of inclusions but greatly increased their average size. Samples acquired near the first-to-freeze end of crystal A-2 exhibited only a few metallic inclusions. Etching these samples at low-current densities caused a mosaic pattern to form on the surface, as shown in Fig. 1-3. This is believed to be due to preferential etching at low-angle grain boundaries.

J. F. Butler
T. C. Harman

D. IMAGING AND STORAGE WITH UNIFORM MOS STRUCTURE

Radiation sensitive characteristics of a uniform InSb metal-oxide-semiconductor structure have been used to detect images. By rapidly optical scanning this structure with visible light of 0.63μ , we have detected infrared images due to $5\text{-}\mu$ radiation. In addition, information can be read in and stored (or "photographed") by using $1\text{-}\mu$ radiation, nondestructively read out with $5\text{-}\mu$ radiation, and erased with $0.25\text{-}\mu$ radiation. Here we discuss some of the results we obtained, along with some of the underlying principles. The principles to be discussed are

Section I

not limited to the use of the InSb MOS structure with its characteristic wavelengths, nor the use of a laser for the optical read-out.

The InSb structure consists of a semitransparent metal film-oxide layer-InSb sandwich. We have previously reported the structure details and the fact that the depletion region in the InSb at the oxide interface could be used as a high quantum efficiency infrared detector.² We also pointed out in the initial report that large area, uniform detectors could be fabricated using an anodization process and a thin metal film evaporation. Here we discuss three effects of radiation at different wavelengths which occur in this structure, and indicate how these effects can be used for detecting images. These three effects are (1) the photovoltaic response of the depletion region in the InSb, (2) the charging of electron states in the oxide or at the InSb-oxide interface by radiation in the vicinity of 1μ , and (3) the modification of these states by ultraviolet radiation, possibly through the induced photoconductivity of the oxide.

To detect infrared images in the vicinity of 5μ , we need only consider the photovoltaic response of the InSb depletion region. Operation in this mode depends on the nonlinear photo-response of the detector which allows the infrared image to influence the signal generated by a scanning laser beam. For an ideal diode, the open-circuit photovoltage is proportional to the logarithm of the photocurrent. With this nonlinear response, a scanning laser beam can in effect saturate a spot on the detector. Electrical isolation from the other areas is provided by the observed high resistivity of the semiconductor depletion region. With no image on the detector, each spot yields the same signal to the external load as its voltage across the depletion region is driven to the saturation value. If the scanning laser beam remains on the active area of the detector, no current flows in the circuit because the detector is capacitively coupled to the load and because the external circuit sees no change of photovoltage as the beam passes across the uniform detector. Should an infrared signal be incident on an element of the detector, this element will contribute less response voltage as the laser scans across it, since there will be less voltage change in driving the element to saturation. This unbalance is detected in the external load. Infrared images have been displayed by synchronizing the horizontal and vertical sweeps of an oscilloscope with the scanning beam and modulating the intensity with the detector signal. By adding the signal to one of the scanning axes, one can obtain a three-dimensional plot for a quantitative record.

Figure I-4 is a photograph of an oscilloscope display of an infrared image formed by the above method. For these results, the InSb structure was cooled to 77°K . The infrared image focused on the structure was confined to radiation in the $4\text{--}5\mu$ interval at an incident power density of $100\mu\text{W}/\text{cm}^2$. The letters of this image were 3 mm high on the detector which had an active diameter of 2 cm. To scan the detector, we used a 1-mW, 0.63μ , helium-neon laser focused to about a 0.3-mm spot. The laser was scanned vertically at 1 kHz and horizontally at 10 Hz, and yielded a reasonably continuous display on the oscilloscope.

Although a number of biasing schemes for enhanced signals could be contrived, in the system used for obtaining the infrared image of Fig. I-4 we applied no bias, but relied on the field-effect bias of the trapped charge in the oxide or at the semiconductor-oxide interface. In fact, the scanning helium-neon laser enhances the amount of trapped charge and fixes it at a steady-state value. This effect of charging up these states, which occurs for wavelengths



Fig. I-4. Oscilloscope display of infrared image.

less than $1.5\ \mu$ (Ref. 3), can also be used to store images. If the MOS structure made with n-type InSb is cooled in the dark, it has very little photoresponse to $5\text{-}\mu$ radiation. If we then form an image on the detector using radiation of wavelengths in the neighborhood of $1\ \mu$, the photoresponse will build up at the locations of the image. The infrared image can then be non-destructively read out using the $5\text{-}\mu$ response of the resulting depletion regions in the semiconductor substrate. This image can be retained for periods in excess of an hour and then erased by raising the detector temperature.

The stored images can also be erased by saturating the entire detector using the $2537\text{-}\text{\AA}$ radiation from a mercury lamp. This modifies the electron population of the interface states such that all elements of the detector are brought to the same responsivity. Following this treatment, a $1\text{-}\mu$ image can again be focused on the detector and read out by scanning with $5\text{-}\mu$ radiation. The ultraviolet radiation corresponds to energies greater than the bandgap of the separate indium and antimony oxides, and probably greater than the corresponding gap of the mixed oxide of our present anodized structure. We believe that in a structure with a $500\text{-}\text{\AA}$ thick oxide, the ultraviolet radiation allows some of the trapped charge to be released. One possible mechanism for accomplishing this could be through the induced photoconductivity of the oxide. For device operation, the important thing is that the photoresponse of a region of the detector to $5\text{-}\mu$ radiation is different depending on what radiation has previously been incident on the detector. The response is different if the element has been equilibrated with $1\text{-}\mu$ radiation than it is if the element has been equilibrated with $2537\text{-}\text{\AA}$ radiation. Since this is the case, it is also evident that one could interchange the roles, reading an ultraviolet image and erasing with diffuse $1\text{-}\mu$ radiation.

Above, we used n-type InSb. If we use p-type InSb, we obtain a negative of the image of the preceding paragraph. When cooled in the dark, the p-type structure shows a response to $5\text{-}\mu$

Section I

radiation, but regions exposed to the $1\text{-}\mu$ radiation lose their response. These results are consistent with previous publications^{3,4} which concluded from measurements of the surface conductance of InSb that illumination of a p-type sample can change the surface from an n-type inversion layer to a p-type accumulation layer. With our present structure, illumination with $1\text{-}\mu$ radiation yields a photovoltage of a polarity indicating a negative charge transfer from the InSb toward the oxide. This photovoltage can be observed at room temperature and is of opposite polarity to the photovoltage developed by the depletion region in the n-type InSb due to $5\text{-}\mu$ radiation. This charge is evidently trapped at low temperatures and causes the field-effect depletion in the InSb. In addition, with the thin $500\text{-}\text{\AA}$ thick oxide we can observe the ultraviolet photoconductivity of the oxide and a further modification of these trapped charges.

R. J. Phelan, Jr.
J. O. Dimmock

E. ION IMPLANTATION

1. Equipment Modifications

Several major equipment modifications have been made in the 400-kV Van de Graaff generator system used to implant heavy ions in semiconducting crystals. Those modifications have been primarily in the vacuum system and in the ion source. The original 2-inch oil diffusion pump was replaced by a turbo-molecular pump which provides a larger pumping capacity and reduces the problem of oil contamination in the drift tube. In addition, an 80-liter/sec Vac-Ion pump was installed directly beneath the sample chamber. The ion source has been modified by replacing the RF oscillator with a more powerful, 90-W, 100-MHz unit, replacing the original plasma bottle with a longer unit, and using an electromagnet to provide the magnetic field for the plasma. The original thermo-mechanically controlled leak for metering the source gas into the discharge tube was replaced by an entirely mechanical leak. The additional power required by the oscillator and electromagnet was provided by replacing the original 300-W alternator in the high-voltage terminal with a 500-W unit.

With these alterations, the modified Van de Graaff generator has operated stably for several 5-hour runs, delivering $1\text{ }\mu\text{A}$ of As^+ ions from a source of AsH_3 , at drift tube and sample chamber pressures of 10^{-6} torr or less.

A. G. Foyt E. D. Hinkley
J. P. Donnelly J. H. R. Ward

2. Ion Implantation of Germanium

We previously reported the conversion of p-type germanium to n-type by implantation with 400-keV phosphorus ions.⁵ With the modified accelerator system described above, further implants of germanium have been performed using arsenic and nitrogen ions. Wafers of 10-ohm-cm p-type germanium were prepared by etch-polishing. For implantation, the wafer was placed on a molybdenum sheet on a copper heat sink and partly covered by a molybdenum mask. A DC bias of +90 V was applied to the sample holder to reduce the secondary electron emission and thereby permit an accurate measurement of the ion current.

A beam of arsenic ions, with a current density of $1\text{ }\mu\text{A}/\text{cm}^2$, was obtained by RF excitation of arsine (AsH_3). Seventeen implants were performed at 400 keV with doses ranging from

2×10^{12} to 1.6×10^{16} ions/cm², and target temperatures ranging from 20° to 500°C. Two types of annealing schedules followed the implants: the first involved 10-minute anneals at various temperatures in a flowing hydrogen gas environment; the second consisted of placing the implanted wafers in an evacuated spectrosil ampoule and inserting the ampoule in a fixed-temperature (490°C) furnace for various lengths of time. Thermal-probe tests and Hall effect measurements using the Van der Pauw technique were performed after each annealing step.

All the 400-keV arsenic implants with the germanium wafers at room temperature required post-implant annealing to produce conversion to n-type conduction. The unimplanted region shows a relatively constant hole concentration independent of annealing. The implanted region also indicates a substantially constant hole concentration to an annealing temperature of 350°C; however, after the 450°C and higher temperature anneals, the Hall coefficient becomes negative, indicating a conversion to n-type conductivity. The maximum electron concentration measured is only slightly below the implanted ion concentration. Most of the implants performed with the germanium wafers elevated to temperatures in the 450° to 500°C range produced n-type conductivity immediately.

A number of implantations of N⁺ in germanium were also performed. The results obtained to date are inconclusive, other than indicating that it is more difficult to obtain type conversion in germanium by implantation of N⁺ ions than it is by implantation of either P⁺ or As⁺.

E. D. Hinkley
W. Matthews

3. Ion Implantation of CdTe

CdTe has been bombarded with the Group V elements, N⁺ and As⁺, which should be p-type dopants. Sample temperatures during implantation have ranged from 4.2°K to 400°C. SiO₂ masking was used for temperatures over 250°C to prevent the loss of Cd from the sample surface. Most recent experiments have been performed at the elevated temperatures. Various post-annealing procedures have been used, including hot-stage annealing with SiO₂ masking, and ampoule annealing with either excess Cd, CdTe powder, or both.

To date, the N⁺ implantation has given no indication of converting CdTe. On the other hand, As⁺ has shown some promising results. Two samples have shown p-type conversion in the implanted layer in both thermal-probe tests and Van der Pauw measurements, whereas the unimplanted sections of these samples were unchanged. Materials problems (especially inhomogeneities in the starting material), however, have hampered the reproducibility of these results. A CdTe annealing program has been initiated to achieve homogeneous starting material.

J. P. Donnelly
A. G. Foyt

REFERENCES

1. M.K. Norr, NOLTR 63-156, U.S. Naval Ordnance Laboratory, White Oak, Maryland (1963).
2. R.J. Phelan, Jr., and J.O. Dimmock, Appl. Phys. Letters 10, 55 (1967), DDC 653365.
3. R.K. Mueller and R.L. Jacobson, J. Appl. Phys. 35, 1524 (1963).
4. G.K. Eaton, et al., J. Phys. Chem. Solids 23, 1473 (1962).
5. Solid State Research Report, Lincoln Laboratory, M.I.T. (1966:4), p. 7, DDC 647688, H-801.

II. OPTICAL TECHNIQUES AND DEVICES

A. STABILITY MEASUREMENTS OF CO₂-N₂-He LASERS AT 10.6- μ m WAVELENGTH

Measurements of the short-term stability¹ of the beat frequency^{2,3} of two stable, single-frequency (TEM_{00q} mode) CO₂-N₂-He lasers have been continued with improved versions of the lasers described previously.^{4,5} Typical Fourier spectra of the beat frequency resembled the discrete line spectrum of a carrier frequency modulated by narrow-band disturbances. The width of the carrier and the dominant sidebands were generally less than the 10- or 20-Hz resolution limit set by the spectrum analyzer, while the total width of the spectrum occupied by all the dominant sidebands was often less than 400 and 200 Hz for observation times of 0.1 and 0.05 sec, respectively. This stability represents considerable improvement over any stability data previously reported for the 10.6- μ m CO₂ laser.

It is well known that the frequency of the laser can be affected by changes in gain. Such gain variations may result from changes in discharge current, or changes in the wall temperature of the discharge tube, etc. For instance, the beat frequency could be easily tuned (or frequency modulated) by changing (or modulating) the power supply voltage, and therefore the discharge current. A typical frequency-pulling figure of 10 kHz/volt was observed at the particular operating point of the laser during such measurements. Since the 60-Hz peak-to-peak power supply ripple, which resembled a noisy square wave, was on the order of 10^{-2} volt, we may

expect the beat note of the lasers to be frequency modulated at the 60-Hz line frequency, with a peak deviation of about 100 Hz. If Δf denotes the peak frequency deviation of the carrier (beat frequency), then the resulting modulation index $\Delta f/f$ would be on the order of one.

Figure II-1 shows a beat frequency spectrum which is dominated by sidebands caused by such frequency modulation at 60 Hz. Note that the spectral widths of the carrier (beat frequency) and the dominant sidebands caused by the 60-Hz modulation fall within the 20-Hz resolution limit of the spectrum analyzer. This indicates a laser stability on the order of 5×10^{-13} for an observation time of 5×10^{-2} sec if we disregard the 60-Hz modulation caused almost entirely by the power supplies used in these measurements. However, even including the 60-Hz/sec modulation, the total width of the beat frequency spectrum would still be only about ten times greater.

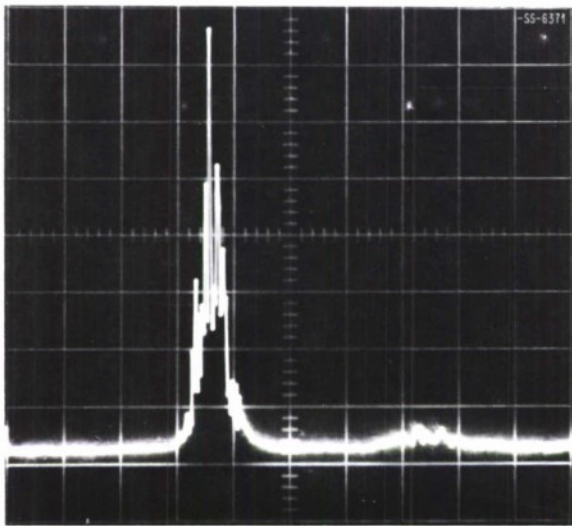


Fig. II-1. Beat frequency spectrum of two lasers: observation time = 5×10^{-2} sec; horizontal scale = 10^3 Hz/cm; vertical scale = linear; resolution = 20 Hz.

Another form of instability appeared as relatively slow beat frequency drifts back and forth at rates varying between tens and hundreds of hertz per second. These drifts were most probably

Section II

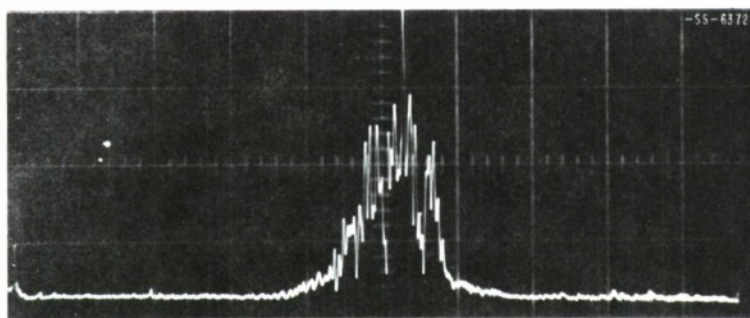


Fig. 11-2(a). Beat frequency spectrum of two lasers: observation time = 10^{-1} sec; horizontal scale = 5×10^2 Hz/cm; vertical scale = linear; resolution = 10 Hz.

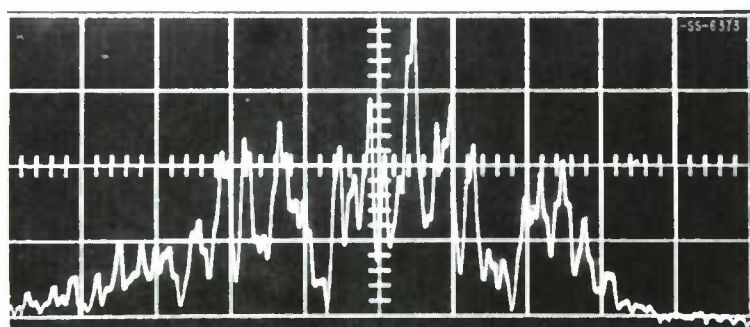


Fig. 11-2(b). X5 magnification of center portion of Fig. 11-2(a): observation time = 10^{-1} sec; horizontal scale = 10^2 Hz/cm; vertical scale = linear; resolution = 10 Hz.

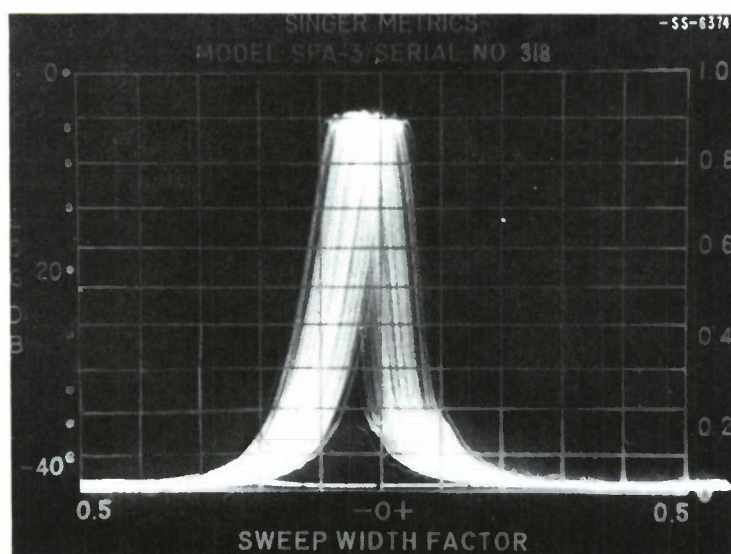


Fig. 11-3. Spectrum analyzer display of beat frequency of two lasers: film exposure time = 4 sec; horizontal scale = 2×10^3 Hz/cm; vertical scale = linear; scanning rate = 60/sec.

caused by gain dispersion due to changes in the wall temperature of the discharge tubes, and by slow changes in power-supply voltages. No serious attempt was made to use either stabilized-temperature and bubble-free coolant or stabilized-temperature power supplies. Figure II-2(a) shows the beat frequency spectrum for an observation time of 0.1 sec with an analyzer resolution of 10 Hz. Figure II-2(b) shows a X5 magnification (100-Hz/division horizontal dispersion) of the center portion of Fig. II-2(a). It is rather clear from Figs. II-2(a) and (b) that the modulation caused by the slow drift and by the line frequency ripple are of the same order of magnitude. However, it should be noted that the slow drift was not monotonic, and the maximum drift in the beat frequency did not exceed 2 to 3 MHz during a full 8-hour working period. Also, this long-term stability was achieved after only a few minutes warmup, with both lasers exposed to the normal laboratory environment on a non-shock-mounted table, and with ordinary tap-water cooling.

Figure II-3 illustrates the effect of drift upon the beat frequency spectrum for an observation time of 4 sec. The total frequency excursion in this figure covers less than 3 kHz for the 4-sec film exposure.

The stability measurements described here were performed during working hours in a fairly normal laboratory environment on the second floor of a building. The lasers were in an acoustically shielded box on a heavy granite slab, but the table was not shock mounted on the usual air mounts. It is believed that the present measurements indicate that another order-of-magnitude improvement in stability could be achieved relatively easily with further improvement of environmental conditions. Thus, it may well be possible to measure the effect of quantum noise on laser stability with the lasers used in these experiments. Calculations indicate that the linewidth imposed by quantum noise upon these lasers is of the order of 10 Hz near the threshold of oscillation.

Both lasers used in these measurements were sealed off and free running without any feedback stabilization. The power output of each laser was of the order of $1\frac{1}{2}$ W, operating in a single TEM_{00q} mode. This power output remained stable even after hundreds of hours of operation, and no problem arose from either multimoding or transition jumping. The detailed construction of these lasers was described previously.^{4, 5} The improvement in stability reported here is attributed mainly to the use of heat-treated and stabilized superinvar rods, and some rudimentary magnetic and thermal shielding of these rods. The coefficient of thermal expansion of the superinvar is at least an order of magnitude better than fused quartz, and passes through zero near room temperature.

C. Freed

B. CONTINUOUS OPERATION OF A SEALED-OFF CO₂ LASER TUBE

A 5-W sealed-off CO₂ laser tube was operated continuously with constant characteristics for 1088 hours, at which time the test was terminated because the NaCl Brewster windows were destroyed by water vapor. This laser was mentioned in the preceding Solid State Research Report,[†] at which time it had operated for 968 hours. A gas sample was taken from this tube at 1088 hours and the analysis showed that 92 percent of the initial concentration of CO₂ still

[†] Solid State Research Report, Lincoln Laboratory, M.I.T. (1967:3), p. 21, DDC 661275.

Section II

remained in the tube, and the major impurity hydrogen was less than 1.5 percent of the total gas concentration. When the tube was disassembled, close inspection of the interior of the nickel cathode indicated a light coating of NiO and carbonates, but generally the cathode appeared almost unused. Except for the hydrogen impurity and its effect on changing the optical output side radiation, the tube probably would operate much greater than the 1000-hour interval. Maintenance of the CO₂ concentration over the indicated time interval has shown that a nickel cathode operated at greater than 300°C will act as a catalyst in converting the CO and O₂ formed in the discharge back into CO₂.

R. Carbone

C. 100-W CO₂ AMPLIFIER AT 10.6 μ m

A 9-meter amplifier composed of three equal-length tubes with bores of 20, 25, and 30 mm is being constructed for use as a 10.6- μ m transmitter. The 25-mm bore tube which is complete has a small signal gain greater than 8 db, which is the estimated gain used in designing this amplifier. Initial measurements indicate that no beam distortion takes place when traversing the tube with a low-power beam.

R. Carbone

REFERENCES

1. Proc. IEEE 54 (February 1966), Special Issue on Frequency Stability.
2. T.S. Jaseja, A. Javan, and C.H. Townes, Phys. Rev. Letters 10, 165 (1963).
3. A.E. Siegman, B. Daino, and K.R. Manes, IEEE J. Quant. Electron. QE-3, 180 (1967).
4. C. Freed, IEEE J. Quant. Electron. QE-3, 203 (1967), DDC 658783.
5. Solid State Research Report, Lincoln Laboratory, M.I.T. (1967:3), p.19, DDC 661275.

III. MATERIALS RESEARCH

A. PbSe-SnSe PSEUDO-BINARY SYSTEM

Because of current interest in the electronic and optical properties of the $\text{Pb}_{1-x}\text{Sn}_x\text{Se}$ alloys,¹ the PbSe-SnSe system has been investigated by differential thermal analysis. The thermal arrests obtained in this investigation are listed in Table III-1, and the eutectic phase diagram based on them is shown in Fig. III-1, where the eutectic temperature is 870 °C. A complete series of solid solutions cannot be formed, since PbSe has the cubic B1 (rocksalt) structure, while SnSe has the orthorhombic B29 structure.

The liquidus and eutectic arrests given in Table III-1 and Fig. III-1 were obtained by cooling curves on initially molten samples. The solidus arrests were obtained from heating curves on solid samples prepared by melting the elements in evacuated fused silica ampoules, quenching in air, crushing, and then homogenizing by annealing in evacuated ampoules for about two weeks at 800 °C. (Figure III-1 also shows several solidus points obtained by electron microprobe analysis of ingots produced by directional freezing.² The position of each such point is given by the composition of the first-to-freeze portion and the liquidus temperature corresponding to the initial melt composition.)

As shown in Fig. III-1, there is a considerable separation between the liquidus and solidus curves for the rocksalt-structure alloys in the PbSe-SnSe system. For the orthorhombic alloys, the separation between liquidus and solidus appears to be negligible, since the eutectic temperature is only 2 °C lower than the melting point of SnSe. This is consistent with the observation that ingots prepared by directional crystallization of melts containing 76, 80, and 90 mole-percent SnSe were uniform in composition along their length to within the error of electron microprobe analysis, which is estimated to be ± 3 percent of the measured composition.

According to the thermal analysis results, at the eutectic temperature the solubility of PbSe in SnSe is 24 mole-percent, in excellent agreement with the value of 25 mole-percent obtained by Krebs, Grün, and Kallen³ from x-ray data on samples annealed at 480 ° to 500 °C. The solubility of SnSe in PbSe at the eutectic temperature is 52 mole-percent, compared with the value of 43 mole-percent determined by Krebs, Grün, and Kallen³ for samples annealed at 550 ° to 580 °C. It is assumed that this difference is due to the decrease in solid solubility with decreasing temperature, and the phase boundary of the solidus has been drawn in Fig. III-1 as a straight line consistent with both solubility values.

A. J. Strauss

B. MAGNETIC PROPERTIES OF SrRuO_3 AND CaRuO_3

In a recent study of the perovskites SrRuO_3 and CaRuO_3 , it was found⁴ that SrRuO_3 is ferromagnetic, with $T_c = 160$ °K, that CaRuO_3 has a negative paramagnetic Curie temperature $\Theta_p = -125$ °K, and that both compounds are good conductors ($\rho \sim 10^{-3}$ ohm-cm) with positive temperature coefficients of resistivity. These observations led us to make a further investigation of the two compounds. Our interest was aroused by three considerations. (1) These materials were expected to offer a good opportunity for studying band magnetism, since their

TABLE III-1 THERMAL ARRESTS IN THE PbSe-SnSe SYSTEM			
Composition (Mole-Percent SnSe)	Temperature (°C)		
	Liquidus	Eutectic	Solidus
0	1085	—	—
10	1064	—	1023
20	1036, 1038	—	990
30	1011	—	949
35	998	—	933
40	980, 984	—	909
45	967	—	895
50	953	867	—
60	921	868	—
70	890	870	—
80	870	—	—
90	870	—	—
100	872	—	—

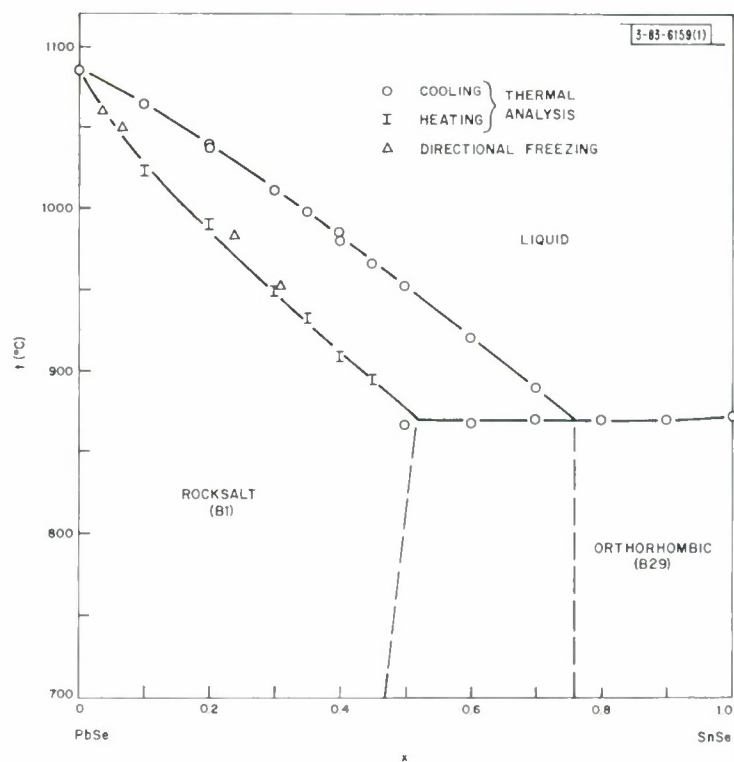


Fig. III-1. Phase diagram of pseudo-binary PbSe-SnSe system.

conductivity appeared to be due to collective rather than localized electrons. (2) Although both compounds have the same number of 4d electrons, one was found to be ferromagnetic and the other to have antiferromagnetic interactions. (3) The ferromagnetic moment measured for SrRuO_3 was lower than the value for the spin-only atomic moment of low-spin Ru^{4+} ions having localized 4d electrons.

Our measurements of the magnetic susceptibility of CaRuO_3 at fields up to 17 kOe essentially confirmed the earlier results⁴ for this compound, which covered the temperature range between 77° and 1000°K. In order to look for evidence of a Néel temperature T_N , the measurements were extended to 4.2°K. Data for a powdered sample are given in Fig. III-2(a-b) which shows a plot of magnetization σ at 4.2°K against applied field H_a , and a plot of reciprocal susceptibility χ^{-1} against temperature. The latter gives clear evidence for a $T_N = 110^\circ \pm 10^\circ\text{K}$, although a well-defined minimum in χ^{-1} is not observed because of the occurrence of a small parasitic ferromagnetism at low temperatures. Such ferromagnetism is commonly exhibited by antiferromagnetic oxides with orthorhombic perovskite structure. The value of the parasitic ferromagnetism σ_0 at 4.2°K is found to be $(3.2 \pm 0.4) \times 10^{-2} \text{ emu/g}$ by application of the usual relationship $\sigma = \sigma_0 + \chi H_a$ to the data of Fig. III-2(a).

Initial measurements on a powdered sample of SrRuO_3 confirmed the earlier⁴ observation of a ferromagnetic moment considerably smaller than the spin-only atomic moment of low-spin Ru^{4+} ions with localized 4d electrons. There are three possible origins for such a reduced

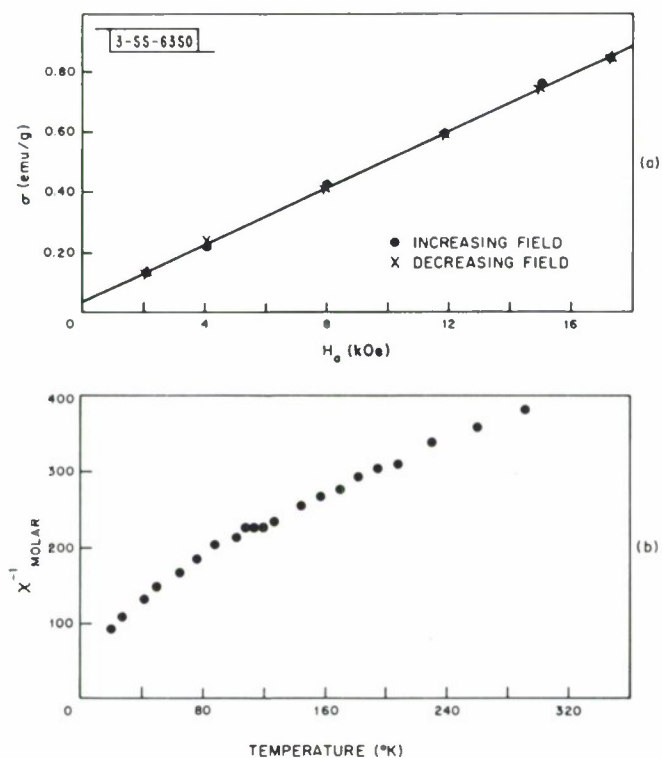


Fig. III-2. Magnetic properties of powdered sample of CaRuO_3 . (a) Magnetization σ at 4.2°K vs applied field H_a ; (b) reciprocal magnetic susceptibility χ^{-1} vs temperature.

Section III

moment: (1) the moment is due to localized 4d electrons, but is decreased by a large crystalline anisotropy which results because the electrons have a relatively large spin-orbit coupling parameter; (2) the spin configuration is complex, consisting of a ferromagnetic and an antiferromagnetic component; (3) SrRuO_3 is a band ferromagnet which has holes in both the spin-up and spin-down bands, in unequal numbers. Since single crystals of SrRuO_3 were not available for anisotropy measurements, an attempt was made to decide between these three alternatives on the basis of data for powdered samples obtained by magnetization measurements at high applied fields and by neutron diffraction experiments.

Magnetization measurements at fields up to 125 kOe were made by S. Foner at the National Magnet Laboratory, M.I.T. He found a ferromagnetic moment of $1.55 \mu_B$ per molecule at 125 kOe and 4.2 °K, compared with the moment of $2 \mu_B$ expected for Ru^{4+} ions with localized electrons. Surprisingly, the magnetization does not appear to be saturated even at the highest fields. This lack of saturation cannot be due to spin canting alone, since σ does not vary linearly with H_a in the high-field region. Further, $d\sigma/dH_a$ at 125 kOe is considerably larger than the slope found at similar fields for metallic iron, where the change in σ is apparently due to a change in the relative populations of spin-up and spin-down bands. This result suggests the presence of a large crystalline anisotropy, or of 4d bands that are much narrower than the 3d bands of iron, or both.

In oxides with localized 3d electrons, a large crystalline anisotropy is generally associated with a distortion of the cationic interstice from cubic symmetry due to ordering of the electrons among the localized orbitals. Below a magnetic-ordering temperature, there is a cooperative distortion of the entire crystal that can readily be detected by x-ray diffraction. X-ray measurements on SrRuO_3 revealed no such distortion below T_c . This observation supports the hypothesis that the apparently metallic conductivity is due to collective rather than localized 4d electrons. However, if there should be a large crystalline anisotropy, its origin would be unknown.

In order to determine whether the reduction in the ferromagnetic moment of SrRuO_3 is due to an antiferromagnetic component in the ordered spin configuration, neutron-diffraction data were collected at the M.I.T. nuclear reactor. A comparison of the diffraction patterns for room temperature and 4.2 °K shows that there are no new peaks at 4.2 °K, and that only the first peak is significantly lower in intensity at room temperature than at 4.2 °K. These observations are consistent with a simple ferromagnetic ordering of the atomic moments on the Ru ions. In good agreement with the value found by the magnetization measurements, a ferromagnetic component of $1.4 \pm 0.4 \mu_B$ per Ru atom was calculated from the intensity difference for the first peak, using the theoretical form factor for a 4d ion obtained by Wilkinson, *et al.*⁵ for Mo^{3+} .

On the basis of all the above observations, we conclude that SrRuO_3 and probably CaRuO_3 exhibit collective-electron rather than localized-electron magnetism, and that there is a sufficient molecular field to make the Curie-Weiss constant approach a localized-electron value. We attribute the difference in magnetic order between SrRuO_3 and CaRuO_3 to the influence of the A^{2+} ions on the widths of the $(\text{RuO}_3)^{2-}$ 4d bands and hence on the relative hole populations of the spin-up and spin-down bands. The presence of holes in both bands presumably accounts for the ferromagnetism of SrRuO_3 . Since a Ca-O bond would have more covalent character than a Sr-O bond, the 4d bands should be narrower in CaRuO_3 than in SrRuO_3 (Ref. 6). This trend

would be consistent with the fact that SrFeO_3 (which has the same number of outer 3d electrons as the number of 4d electrons in SrRuO_3 and CaRuO_3) is antiferromagnetic below $T_N \approx 130^\circ\text{K}$ (Ref. 7), since the 3d bands in SrFeO_3 should be narrower than the 4d bands of SrRuO_3 (Ref. 8).

J. M. Longo
P. M. Raccach
J. B. Goodenough

C. PRESSURE DEPENDENCE OF MAGNETIC TRANSITIONS IN SPINELS

The Curie temperature T_c has been measured as a function of hydrostatic pressure up to 6 kbars for the magnetic spinels CuCr_2S_4 , CuCr_2Se_4 , and CdCr_2Se_4 . Both CuCr_2S_4 and CuCr_2Se_4 exhibit metal-like electrical behavior (the resistivity is small and has a positive temperature coefficient), while CdCr_2Se_4 is a semiconductor. In all three cases, T_c decreases linearly with increasing pressure over the pressure range investigated. The measured values of dT_c/dP are listed in Table III-2.

TABLE III-2 PRESSURE COEFFICIENTS OF THE CURIE TEMPERATURE IN SPINELS		
Compound	T_c at 1 atm (°K)	dT_c/dP (deg/kbar)
CdCr_2Se_4	133	-0.85
CuCr_2Se_4	429	-0.45
CuCr_2S_4	375	-1.39

For CdCr_2Se_4 , the negative sign of dT_c/dP indicates that a reduction in lattice size increases the antiferromagnetic direct superexchange interaction between B-sites more rapidly than it increases the ferromagnetic 90° superexchange interaction between these sites.

The same mechanism is presumably operating in the two spinels containing Cu. In this case, however, the situation is complicated by the presence of band electrons, which can also give rise to a negative pressure coefficient. The magnitude of the effect due to band electrons should be similar in the two compounds. Therefore, the fact that the absolute value of dT_c/dP is about three times as great for CuCr_2S_4 as for CuCr_2Se_4 indicates that the magnitude of dT_c/dP is primarily determined by the superexchange interactions involving the localized B-site moments. This conclusion is consistent with the fact that the compound with smaller cell size (CuCr_2S_4) has the larger absolute value of dT_c/dP .

J. A. Kafalas K. Dwight, Jr.
N. Menyuk J. B. Goodenough

D. CONSTRUCTION OF AN ELECTRONIC PHASE DIAGRAM

It now appears possible to distinguish at least four general electronic phases: (1) localized electrons, (2) collective electrons exhibiting a spontaneous magnetic ordering at lower

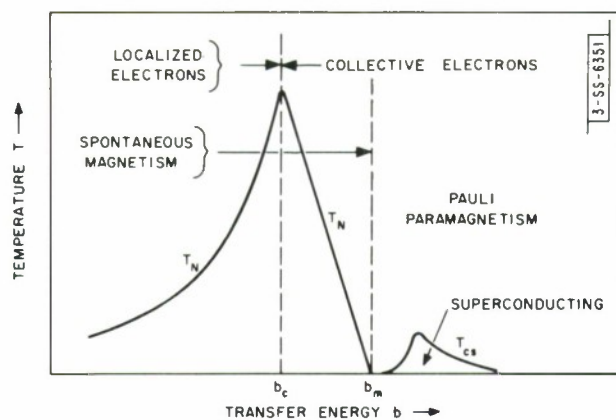


Fig. III-3. Schematic electronic phase diagram for one electron per orbital ($n_d = 1$).

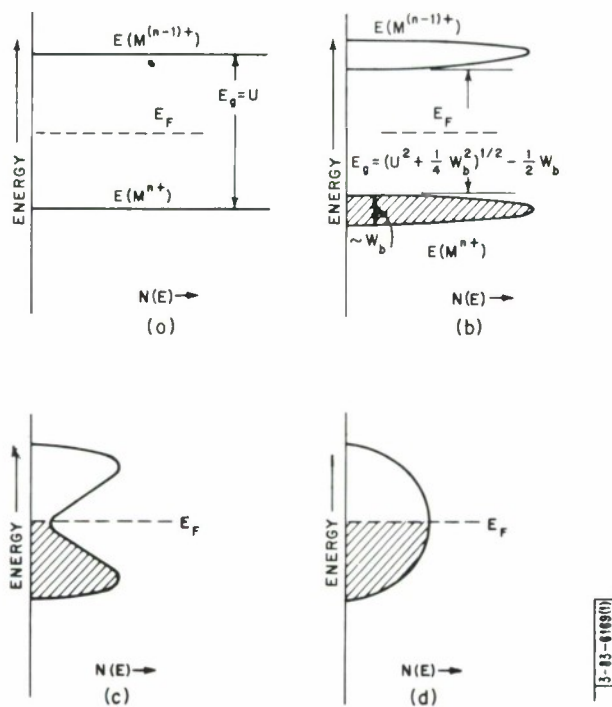


Fig. III-4. Density of states vs energy as function of transfer energy b , where U is intra-atomic Coulomb energy ($U \neq$ Hund splitting). (a) $b < b_c$; (b) $b \approx b_c$; (c) $b \approx b_m$; and (d) $b > b_s$.

temperatures, (3) collective, normal-conducting electrons having no spontaneous magnetization, and (4) collective, superconducting electrons. It is therefore meaningful to construct a qualitative electronic phase diagram as a function of suitable physical parameters to guide future experimentation.

Two obvious parameters are temperature T , and the number of electrons per relevant orbital n_d . The notation n_d reflects the fact that, in general, only outer d electrons are intermediate in character, being localized in some crystals and superconducting in others. A possible third parameter is the ratio b/U , where b is the one-electron transfer integral appearing in tight-binding collective-electron theory (bandwidth $W_b \sim b$) and in localized-electron superexchange theory (exchange energy $J \sim b^2/U$). The Coulomb energy

$$U = (|\phi_m(1)|^2, V|\phi_m(2)|^2) \quad ; \quad V = (e^2/r_{12}) \exp[-\xi r_{12}] \quad (1)$$

contains a screening term $\xi = \xi(b)$, so that it may be expected to decrease rapidly with increasing b through the range of b of critical interest. This means that the perturbation superexchange energy $\sim b^2/U$ increases rapidly with increasing b , breaking down at some critical value b_c that is sharply defined. It also suggests that the transfer energy b , rather than the ratio b/U , should be taken as the third significant physical variable.

The Stoner criterion for spontaneous band magnetism is

$$U \cdot N(E_F) \geq 1 \quad (2)$$

where the density of states at the Fermi surface, $N(E_F)$, not only depends on n_d and the band shape, but also is inversely proportional to the bandwidth $W_b \sim b$. Thus, again, the critical variable is b/U , which decreases rapidly with increasing b through the critical b_m , and it is reasonable to anticipate that the interval $b_c < b < b_m$ is relatively small. Presumably, this is the reason that spontaneous band magnetism occurs rarely among the elements of the periodic table.

Two physical conditions must be distinguished: an integral n_d , and a nonintegral n_d . For $n_d = 0$ or 2 , the relevant orbitals are either empty or filled. Therefore, the only nontrivial integral n_d is $n_d = 1$, corresponding to half-filled orbitals. From the rules for superexchange, overlapping half-filled localized orbitals couple antiferromagnetically. From the narrow-band Jahn-Teller theorem, spontaneous magnetism among collective electrons in a half-filled band gives antiferromagnetic order. Thus, there is no discontinuity in the magnetic order on going from $b < b_c$ to $b > b_c$. However, the Néel temperature is $T_N \sim b^2/U$ for $b < b_c$, whereas T_N decreases continuously to zero with increasing b throughout the range $b_c < b < b_m$. Finally, the superconducting transition temperature T_{cs} , which is proportional to $N(E_F) \sim 1/b$ where $U \approx 0$, can be expected to rise fairly steeply to a maximum value with increasing b for $b > b_m$, as shown schematically in Fig. III-3. Schematic energy diagrams corresponding to different values of b are shown in Fig. III-4(a-d).

For a nonintegral $n_d = 1 \pm c$, the c itinerant electrons or holes couple the localized electron per orbital ferromagnetically via double exchange, where $\epsilon_D \sim cb \cos(\Theta/2)$. Since the superexchange energy is $\sim (b^2/U) \cos \Theta$, minimization of the total energy with respect to Θ gives a canted-spin configuration having both a ferromagnetic and an antiferromagnetic component. Thus,

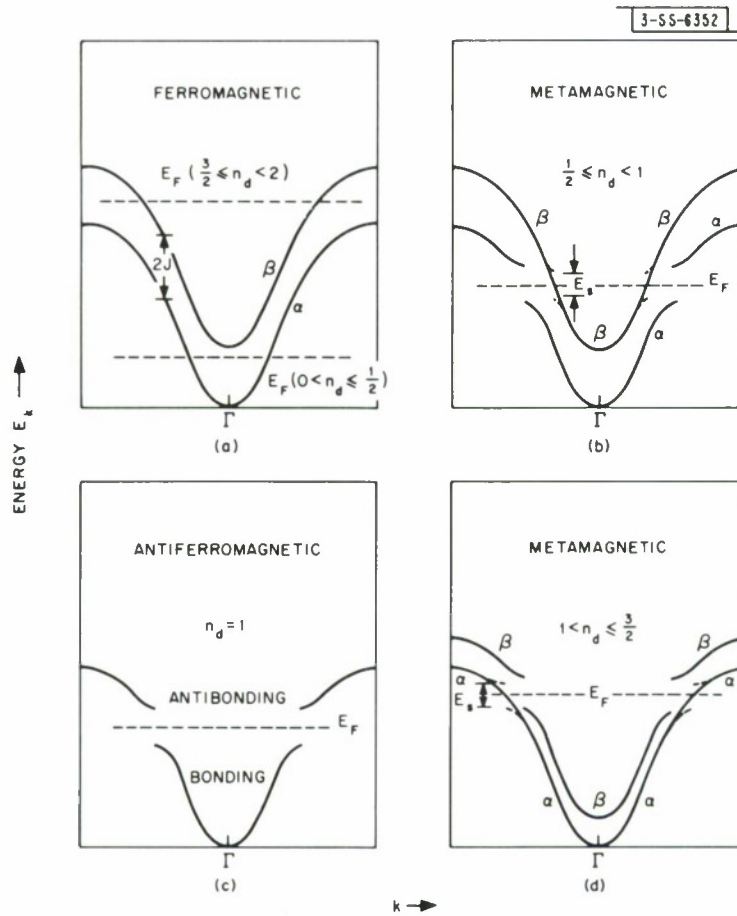


Fig. III-5. Energy band splittings due to spontaneous band magnetism. In (b) and (d), ferromagnetism may be stable at all T ; where antiferromagnetism is stable, antiferromagnetic \rightleftharpoons ferromagnetic transitions may be induced by an increase in T if $T_N < T_C$, and/or by an applied field.

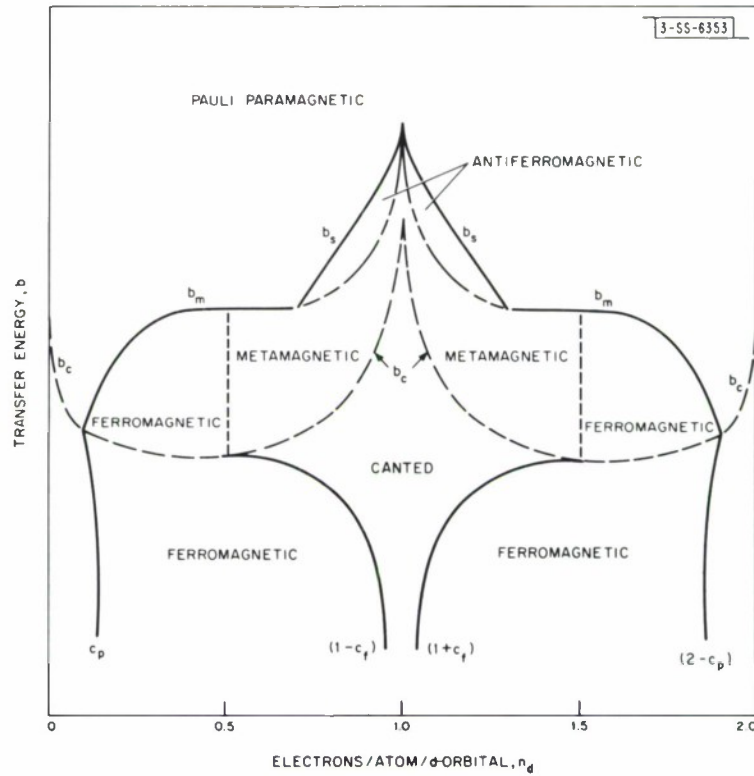


Fig. III-6. Schematic electronic phase diagram of b vs n_d . Axis $n_d = 1$ corresponds to Fig. III-3, with temperature axis perpendicular to plane of paper. Regions designated metamagnetic correspond to Figs. III-5(b) and (d).

as the fraction c of itinerant electrons is increased, the ferromagnetic component increases continuously until simple ferromagnetic order is reached for $c > c_f \sim |J|/b \sim b/U$. In the range $b_c < b < b_m$, there is a minimum in $N(E)$ vs E corresponding to $n_d = 1$ as a result of the Coulomb energy U , and the spontaneous magnetization is as shown schematically in Fig. III-5(a-d). For $n_d \leq 1/2$ and $n_d \geq 3/2$, the magnetic order is unambiguously ferromagnetic and the atomic moment is $\mu = n_d \mu_B$ or $(2 - n_d) \mu_B$, respectively. In the intermediate range $1/2 < n_d < 3/2$, any ferromagnetic component is reduced: $\mu = (1 - n_d) \mu_B$ for $1/2 < n_d \leq 1$, and $\mu = (n_d - 1) \mu_B$ for $1 \leq n_d < 3/2$. There is also the possibility of an antiferromagnetic \leftrightarrow ferromagnetic transition, a spiral-spin configuration occurring at lower temperatures.

Figure III-6 is a schematic electronic phase diagram showing b vs n_d , where b_m is determined from Eq. (2) given a parabolic energy band, and b_s is given by the criterion for an Overhauser spin-density wave:

$$U \cdot F(\underline{q}_0) \geq 1 \quad ; \quad F(\underline{q}) = \frac{2\Omega}{(2\pi)^3} \int_{E_{\underline{k}} < E_F} d^3 \underline{k} / (E_{\underline{k}+\underline{q}} - E_{\underline{k}}) \quad (3)$$

and $F(\underline{q})$ is a maximum at $\underline{q} = \underline{q}_0$.

J. B. Goodenough

REFERENCES

1. J.O. Dimmock, I. Melngailis, and A.J. Strauss, Phys. Rev. Letters 16, 1193 (1966), DDC 642225.
2. T.C. Harman, personal communication.
3. H. Krebs, K. Grün, and D. Kallen, Z. anorg. u. allgem. Chem. 312, 307 (1961).
4. A. Callaghan, C.W. Moeller, and R. Ward, Inorg. Chem. 5, 1572 (1966).
5. M.K. Wilkinson, E.O. Wollan, H.R. Child, and J.W. Cable, Phys. Rev. 121, 74 (1961).
6. J.B. Goodenough, Phys. Rev. 164, 785 (1967).
7. J.B. MacChesney, R.C. Sherwood, and J.F. Potter, J. Chem. Phys. 43, 1907 (1965).
8. J. B. Goodenough, Czech. J. Phys. B17, 304 (1967).

IV. PHYSICS OF SOLIDS

A. ELECTRONIC BAND STRUCTURE

1. Electroabsorption in Bulk Single Crystals of Germanium

Electroabsorption measurements have previously been carried out¹ on semiconductor samples by either placing the electrodes directly on the samples or by obtaining a sample containing a grown p-n junction. The former technique is limited to high-resistivity materials or to low temperatures, while the latter is limited to the few materials which can be obtained with the appropriate configuration. We have adapted the previously reported technique² for making electroreflectance samples to a configuration for making transmission measurements, and have been able to make electroabsorption measurements on bulk single-crystal samples over the temperature range from 5° to 300°K.

The sample configuration is illustrated in the inset of Fig. IV-1. The transmission sample is ground and polished to the desired thickness and then is electrically and mechanically connected to the substrate mask with a thin coat of silver-conducting epoxy. The substrate is a thicker piece of the same material as the sample in order to eliminate any strains induced by differential thermal expansion. The sample is then coated with an insulating layer of Kodak photoresist (KPR) and electrical contacts are made to a semitransparent nickel film evaporated onto the insulating layer; the substrate is used as the other electrode.

The first results, obtained on an n-type germanium sample $\sim 125\mu$ thick, are shown in Figs. IV-1 and IV-2. Figure IV-1 is a typical trace of the normalized electroabsorption signal $\Delta T/T$ obtained by scanning through the energy range of the indirect and direct absorption edges in germanium at a temperature of 200°K. Since the absorption is very large at the direct edge in a sample of this thickness, only the first half of the direct edge line is seen before the transmission signal is too weak to detect. The indirect line shape is clearly resolved on the side of the direct edge signal and is smaller by a factor of 500. The line at 0.73 eV corresponds to the indirect edge energy [$\xi(\Gamma_{25}') - \xi(L_1)$] plus the energy of an LA phonon. The weaker line at 0.68 eV gives the indirect gap energy minus the energy of the absorbed LA phonon. At lower temperatures, we have also seen the TA phonon lines, but they are not very well resolved for these modulation conditions. The line position, when taken as the point of steepest slope of the 0.73-eV line, is measurable to within the instrument resolution of about 1 meV.

This high accuracy of measurement enables us to make an accurate determination of the temperature coefficient of these energy gaps, as illustrated in Fig. IV-2. The major source of error is in the temperature measurement. The half-height points of the phonon absorption line are used to delineate this line shift with temperature.

Aside from making possible an accurate determination of the dependence of the gaps on various parameters, with a significant increase in sensitivity, this technique also allows a study of the line shape of electro-optical signals. The samples are usable both for electroreflectance and electroabsorption measurements. We are now making such measurements simultaneously

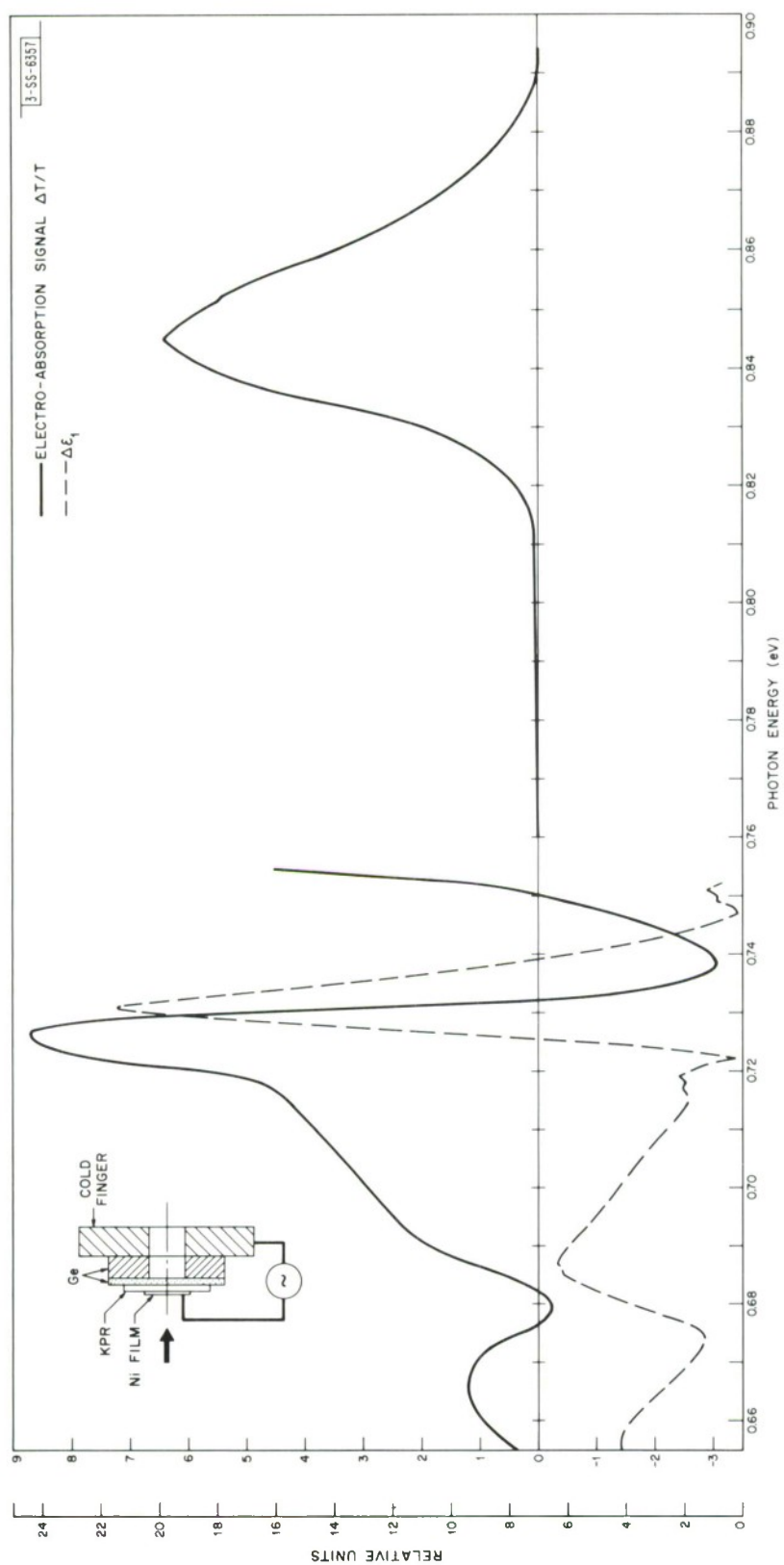


Fig. IV-1. Electroabsorption signal ($\Delta T/T$) in 125- μ thick germanium sample at 200°K. The Kramers-Kronig inversion signal $\sim \Delta \epsilon_1$ is also shown in relative units. Indirect edge signal magnified 500X relative to direct edge. High energy side of direct edge is distorted by instrument limitations.

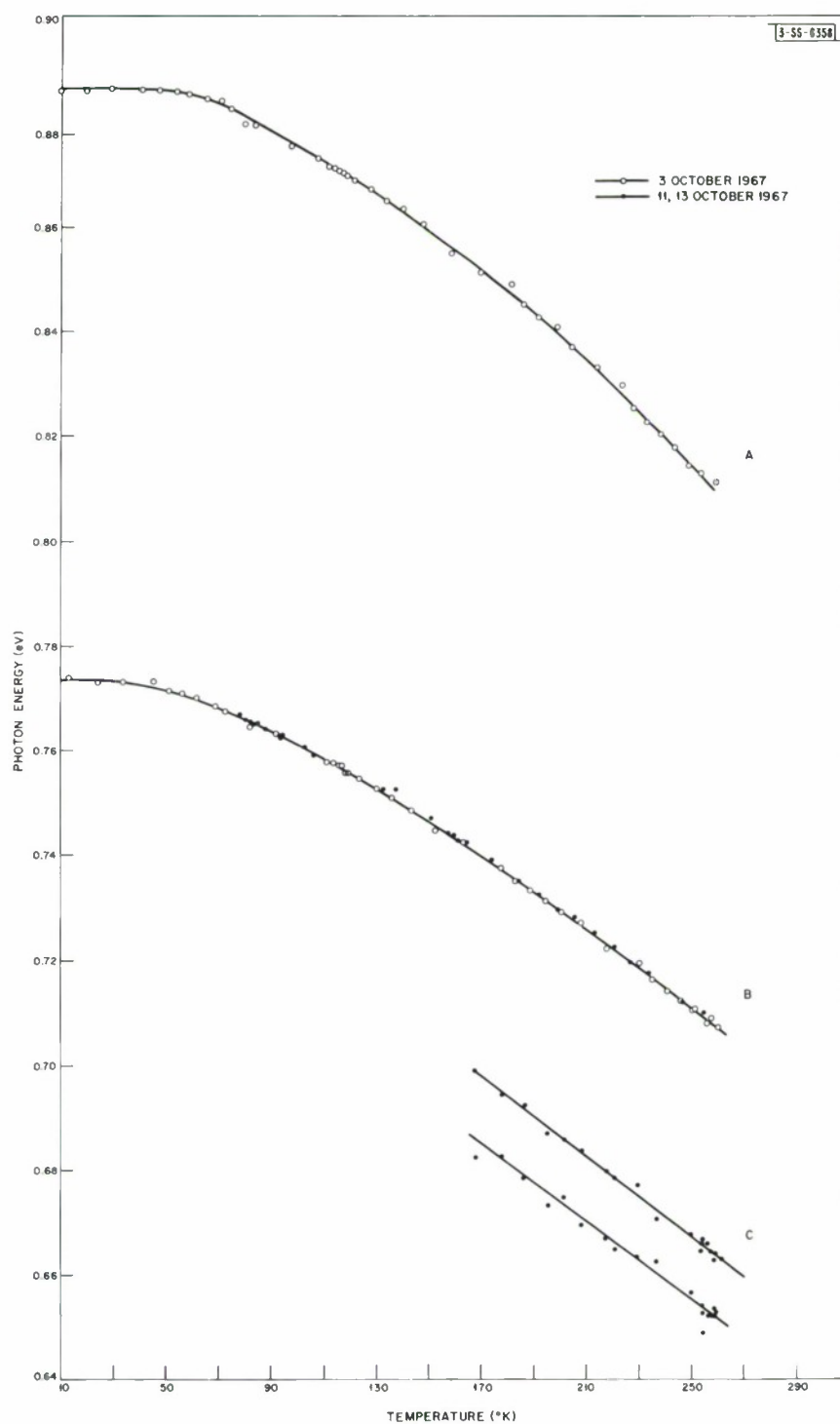


Fig. IV-2. Temperature shift of electroabsorption of direct edge A, and of LA phonon-assisted indirect absorptions B and C. B is taken at point of maximum slope, and C is delimited by half-width points of electroabsorption signal. Curves are composite of several runs, and indicated points show low scatter in data.

Section IV

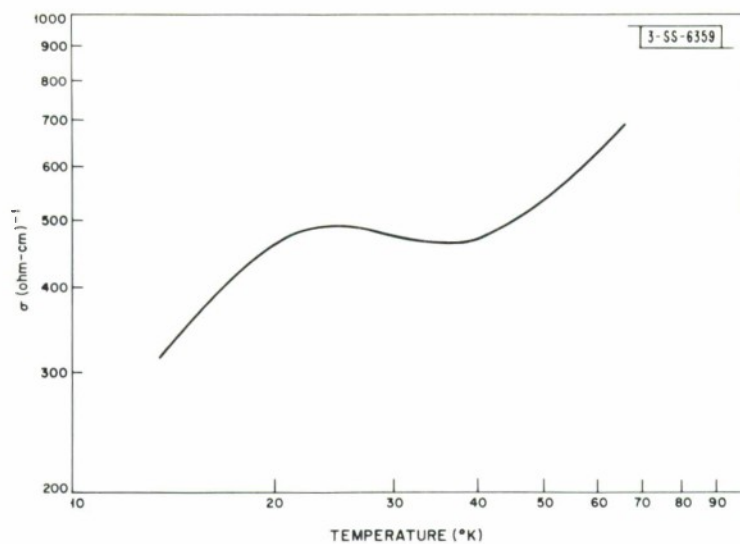


Fig. IV-3. Conductivity vs temperature for pure HgTe sample.

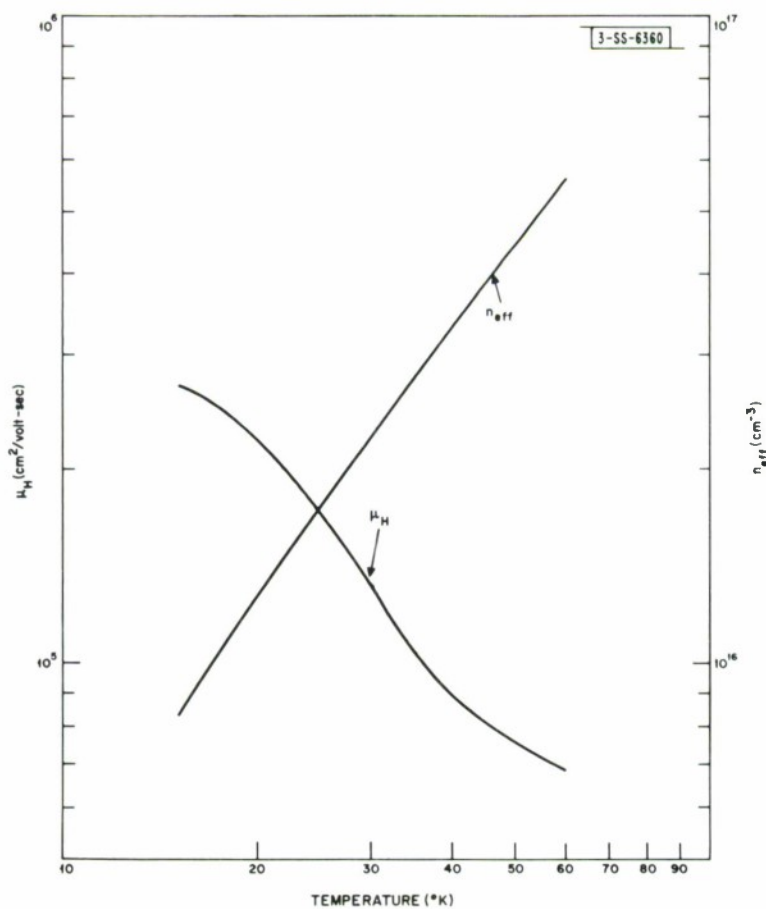


Fig. IV-4. Temperature variation of n_{eff} ($\equiv 1/Re$) and μ_H ($\equiv R\sigma$) for sample in Fig. IV-3.

and are comparing the data by means of the Kramers-Kronig transforms of the modulated absorption and reflection signals.

J. Feinleib
B. Feldman

2. Unusual Temperature Dependence of Conductivity in HgTe

Recently, Ivanov-Omskii, et al.,³ have reported measurements of the conductivity of HgTe as a function of temperature. For high-purity samples, they observed a plateau in the vicinity of 20° to 30°K. This plateau disappears in magnetic fields greater than about 1000 Oe, and is not observed for less pure samples. The authors suggest that the plateau may be caused by a transition from an excitonic insulator to a semimetal, and that the dependence upon doping and magnetic field is in qualitative agreement with this explanation.

Since the conductivity σ is proportional to the product of the carrier concentration n and the mobility μ , we have measured the temperature dependence of n and μ as well as σ in order to investigate the significance of the reported plateau. Figure IV-3 shows the conductivity vs temperature for an undoped sample of HgTe, and is essentially the same as reported for pure samples in Ref. 3. In Fig. IV-4, we plot the temperature dependence of the effective carrier concentration n_{eff} ($\equiv 1/Rc$) and the Hall mobility μ_H ($\equiv R\sigma$), where R is the Hall coefficient. Although the sample is close to intrinsic even at the lowest temperatures measured here, the low-field Hall coefficient gives the electron concentration because the electron mobility is much larger than the hole mobility. Our measurements were made at about 280 Oe, which is well below the field where the conductivity plateau disappears.

Several features of Fig. IV-4 are of interest. First, the carrier concentration increases smoothly with temperature with a dependence slightly weaker than $T^{3/2}$, the dependence for intrinsic activation across a zero energy gap. Other authors have reported a similar variation in carrier concentration for HgTe (Refs. 4 and 5). The mobility decreases smoothly at about the same rate as the concentration increases in the region of the conductivity plateau, and less rapidly at higher and lower temperatures. Thus, the plateau apparently arises merely because the temperature dependences of the mobility and electron concentration happen to cancel over a certain range of temperature. We have not analyzed the temperature dependence of the mobility in terms of various scattering mechanisms. We expect, however, that the scattering of electrons by holes should be important, and this will cause the electron mobility to decrease with temperature because of the increase in hole concentration due to thermal activation. For this type of scattering, both the mobility and the temperature dependence of the mobility will depend quite strongly on the doping of the sample.

When the electron mobility is high and there are roughly equal concentrations of electrons and holes, the resistivity increases rapidly with magnetic field. At higher temperatures, the reduced electron mobility causes a slower change of resistance with magnetic field. Thus, it is reasonable to expect the conductivity-vs-temperature curve to be dependent upon magnetic field.

In summary, our measurements suggest that the plateau in conductivity can be attributed to a reasonable variation in carrier concentration and mobility with temperature. At the very

Section IV

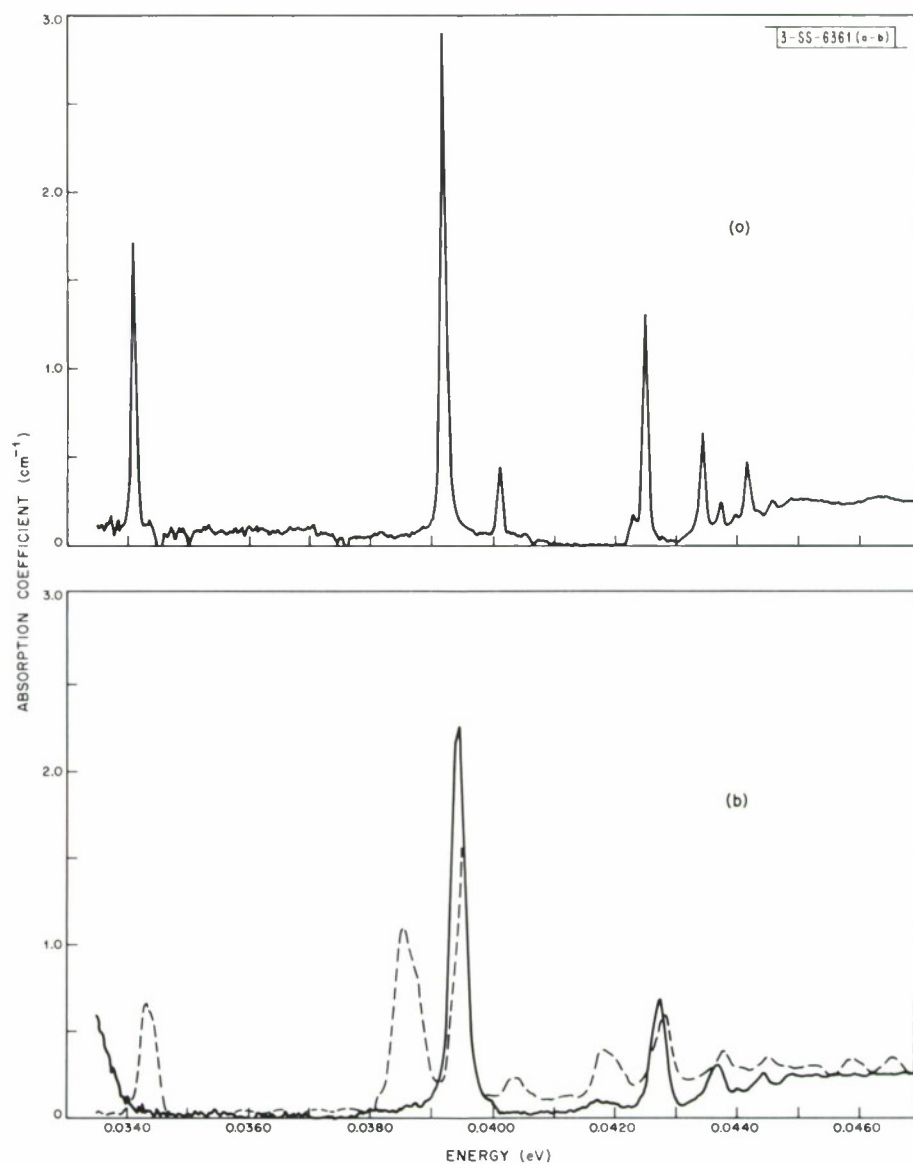


Fig. IV-5. Absorption spectrum of phosphorous impurity in silicon at $\approx 10^\circ\text{K}$ with (a) no applied stress, unpolarized radiation, and (b) $[001]$ applied stress (1.16×10^8 dynes/cm²); solid line — radiation polarized parallel to applied stress, dashed line — radiation polarized perpendicular to applied stress ($\vec{E} \parallel [110]$).

least, this explanation must be discounted in detail before any case can be made for an excitonic insulator-semimetal transition.

S. H. Groves
F. T. Smith
A. J. Strauss

3. Effects of Calibrated Uniaxial Stress on Impurity Spectrum of Phosphorous-Doped Silicon

Measurements of the effect of a calibrated uniaxial stress on phosphorous-doped silicon have been completed. Figure IV-5(a) shows the zero stress absorption, and Fig. IV-5(b) shows the effect of an [001] stress on the absorption spectrum of the $1s \rightarrow np$ transitions for phosphorous. For Fig. IV-5(b), the stress had a value of 1.16×10^8 dynes/cm². The results are as expected for a simple substitutional donor in the silicon lattice on the basis of the effective mass theory. These results, and those for stress in the [111] and [110] directions, are in good agreement with the experiments of Aggarwal and Ramdas.⁶ In addition, with a calibrated uniaxial stress we are able to measure the pure shear deformation potential of the conduction band edge minima.⁷ The shift and splitting of various transitions are shown in Fig. IV-6. We measure a value for the pure shear deformation potential $E_2 = 7.9 \pm 0.2$ eV, in agreement with the value previously measured using sulfur-doped silicon.⁷

W. E. Krag

4. Automatic Recording of Spectrometer Data

A system for automatically recording spectrometer data has been devised, built, and placed into operation in the laboratory. Programs have been written for processing data in the form of successive traces of sample-in sample-out, intensity-vs-wavelength recordings.

A block diagram of the system is presented in Fig. IV-7. The Vidar Data Acquisition System consists of a scanner, an integrating digital voltmeter, and a coupler. An output signal is provided for transmission to the Laboratory computing facility by means of a Western Electric 403A2 data set operating at 200 bits/sec over a standard switched voice grade telephone circuit.

Presently, the system is being fed from a modified Perkin-Elmer infrared spectrometer. The detector signal is amplified by a Princeton Applied Research model HR-8 phase sensitive amplifier, whose output is fed to the scanner and also to a standard chart recorder. The scanner controls the sampling rate, up to almost four points per second, and will handle up to ten channels of data. At present, we are using only one channel, with the channel number being used for identification of data. The signal goes to the digital voltmeter, and then to the coupler which serializes the data for transmission through the data set and telephone line to an IBM 2702 Data Transmission Control which, in turn, couples the data to an IBM 360/40 computer handling many jobs in parallel under multiprogrammed control. The 360/40 computer does some preliminary processing and puts the data onto magnetic tape in a form suitable for further processing.

The data on the tape consist of all the data points, collected at a rate of about 4/sec for the entire duration of the experimental run. Data points taken between drum scans are marked to delineate the useful data. The wavelength marker signal from the scanning drum of the spectrometer is used to label those data points which are coincident with the marker. An accurate log of the operation is made since the data processing programs specifically require that all

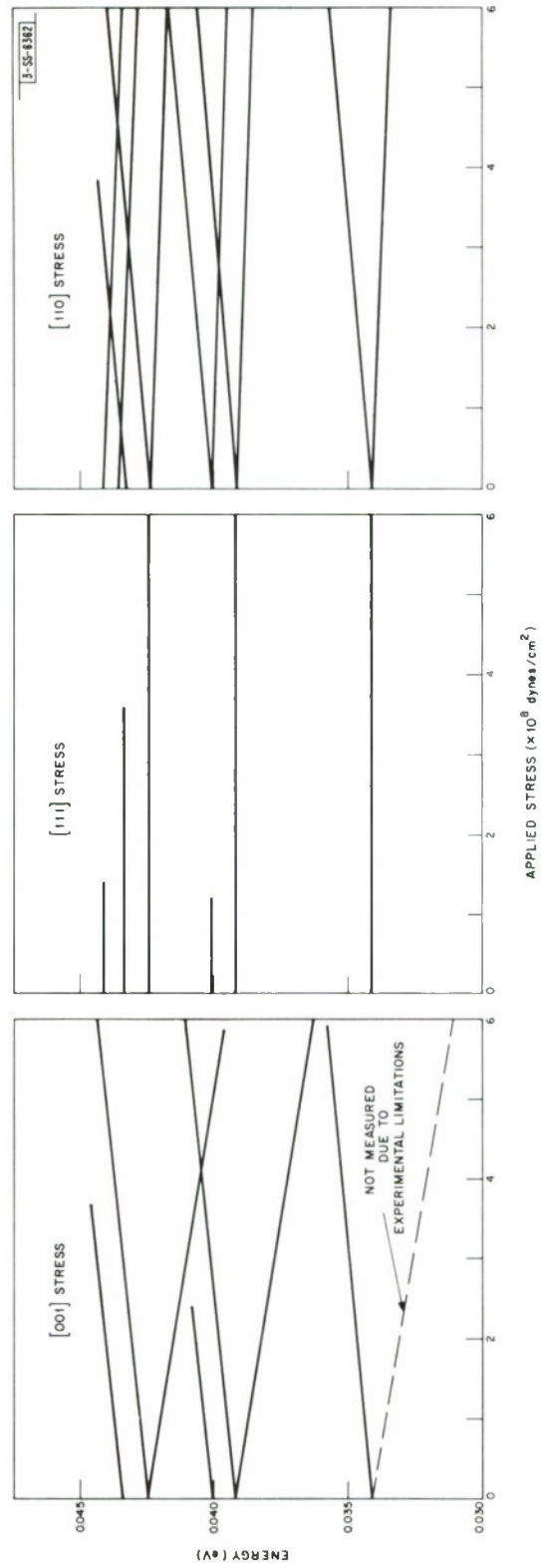


Fig. IV-6. Effect of applied uniaxial stress on transition energies of phosphorous in silicon.

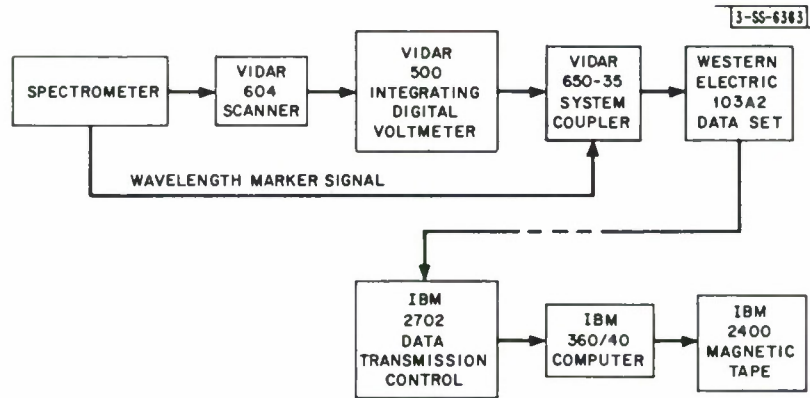


Fig. IV-7. Block diagram of data acquisition and processing system.

wavelength scans be identified and that the wavelength dial number at the beginning of a scan, the channel number, and the gain setting of the amplifier also be given for each scan. With the present data generation rate and packing density, a reel of tape will hold approximately 24 hours of data.

The experimentally derived data are processed on an IBM 360/67 to give tabular data in the form of transmission ratio vs drum number, or photon energy. The results can also be plotted by a Stromberg-Carlson 4020 plotter. An example of the processed data in the form of I/I_0 vs photon energy is shown in Fig. IV-8. The data, taken at about 10°K show the $1s \rightarrow 2p_0$ and $1s \rightarrow 2p_{\pm}$ transitions in a silicon sample doped with a phosphorous concentration of $\approx 10^{14}$ atoms/cm³. The same I/I_0 data, converted to absorption coefficient, are plotted in Fig. IV-9.

W. E. Krag R. N. Davis†
N. L. Daggett† F. E. Perkins‡

5. Analysis of Landau Levels in InSb

The previously observed⁸ fine structure in the interband magnetoabsorption of InSb has established the existence of exciton effects in these transitions and has provided a means of checking the theory of exciton energy levels in a magnetic field. With an exciton theory that has been confirmed by experiment, we have been able to correct the experimentally observed transition energies for excitons and focus our attention on a study of the Landau levels. In the absence of nonparabolic effects, one can write the corrected transition energies as

$$h\nu_n = \epsilon_g + [(2n + 1) \frac{m}{\mu} \pm \frac{1}{2} g_R] \beta H \quad (1)$$

where ϵ_g is the energy gap, n is an integer, μ and g_R are, respectively, a reduced conduction-valence band effective mass and a reduced conduction-valence band g -factor, i. e.,

$$\frac{1}{\mu} = \frac{1}{m_e} + \frac{1}{m_h} \quad (2)$$

and

† Group 28.

‡ Presently at the Department of Civil Engineering, M.I.T.; formerly of Group 28.

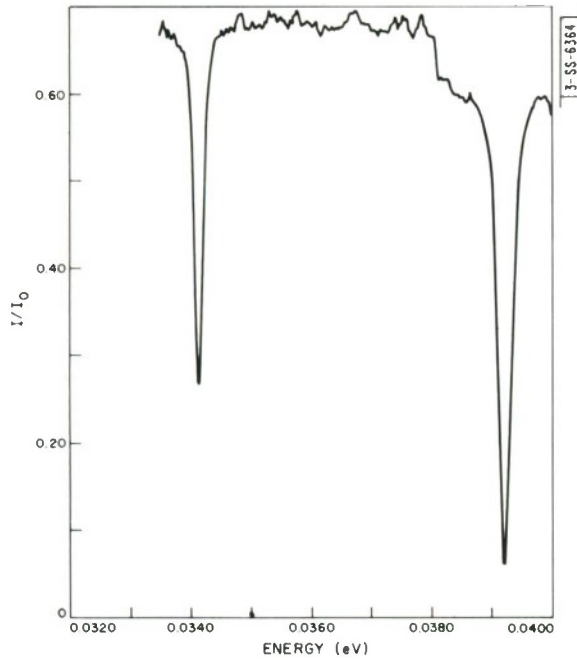


Fig. IV-8. Transmission vs energy for phosphorous-doped silicon.

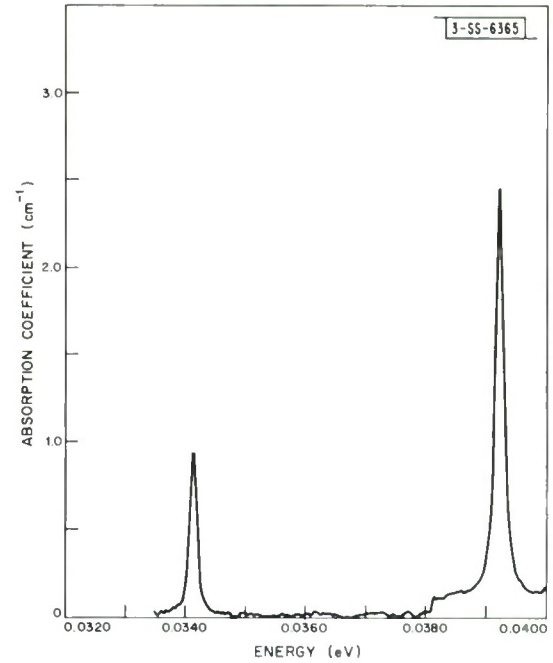


Fig. IV-9. Absorption coefficient vs energy for phosphorous-doped silicon.

$$g_R = g_C \pm g_V \quad (3)$$

We have examined the two lowest transitions in the $E \parallel H$ spectrum of InSb which correspond to $n = 0$. Below about 15 kG, nonparabolic effects are not significant and the data can be analyzed using the above equations. At about 20°K, we obtain $\epsilon_g = 236.7$ meV, $\mu = 0.0137$ m, and $g_R = 48.4$. A comparison with the conduction band $m_e = 0.0138$ m as determined by cyclotron resonance,⁹ and $g = 48.4$ as determined by combination resonance,¹⁰ leads to the conclusion that the valence band levels do not move significantly with magnetic field.

At higher magnetic fields, the nonparabolic effects of the conduction band can be taken into account using the Bowers and Yafet theory.¹¹ Pidgeon and Brown¹² have improved upon this theory; however, we have found that conduction band Landau levels for magnetic fields to 40 kG,[†] as determined by Pidgeon and Brown, are not significantly different from those of Bowers and Yafet.

Using the Bowers and Yafet theory, we have calculated the energy (as measured from the top of the valence band at $H = 0$) of the lowest two conduction band Landau levels for magnetic fields to 40 kG. We compared these calculated energies with the respective observed interband transition energies. Below about 10 kG, the calculated and observed energies are approximately equal, confirming that the top of the valence band does not move much with magnetic field at low magnetic fields. At higher magnetic fields, the observed energies increase with magnetic field faster than the calculated energies. At 40 kG, the difference in energy observed is comparable to that expected for the shift of the valence band levels from the theory of Pidgeon and Brown.

[†] It is a pleasure to acknowledge the assistance of S. H. Groves in making this comparison.

The observed behavior of the top of the valence band at low magnetic fields cannot be easily explained; it appears to be connected with the fact that the top of the valence band in InSb is not expected to occur at $\vec{k} = 0$ (Réf. 13). This effect should disappear for magnetic fields such that the energy difference between valence band Landau levels is much greater than the separation between the top of the valence band and the value at $\vec{k} = 0$ (estimated to be ~ 0.1 meV).

E. J. Johnson

6. Polaron Ground State Energy

We have developed a variational trial function for the polaron problem which gives (a) the exact ground state energy through order α^2 at weak coupling, (b) energies lower than the Feynman theory for $\alpha \leq 3$, and (c) energy higher than that calculated from the Feynman theory but lower than the Low-Pines energy for $\alpha = 5.2$. This theory has the advantage that, unlike the Feynman method, the connection with the ordinary quantum mechanical picture of the polaron is clear, and the energies can be calculated numerically in a matter of seconds on the IBM 360/65. Furthermore, the theory can be extended, at the cost of considerable labor, to calculate variationally the polaron energy for low polaron momentum. Thus, "variational" effective masses, expected to be of high accuracy for $\alpha \lesssim 4$, can be calculated. This is important because measurements are now becoming available¹⁴ of polaron masses in the silver halides ($\alpha = 1$ to 2) and the alkali halides ($\alpha = 2.5$ to 7).

If we write the polaron Hamiltonian in the form it takes after the LLP ground state transformation, we have¹⁵

$$H = (p - \sum_{\vec{k}} n_{\vec{k}})^2 + \sum_{\vec{k}} n_{\vec{k}} - \alpha - 2p \cdot \sum_{\vec{k}} f_{\vec{k}} (b_{\vec{k}}^+ + b_{\vec{k}}) + 2 \sum_{\vec{k}} \cdot \sum_{\vec{k}'} f_{\vec{k}} f_{\vec{k}'} b_{\vec{k}}^+ b_{\vec{k}'} \\ + \sum_{\vec{k}} \cdot \sum_{\vec{k}'} f_{\vec{k}} f_{\vec{k}'} (b_{\vec{k}}^+ b_{\vec{k}'}^+ + b_{\vec{k}} b_{\vec{k}'} + 2 \sum_{\vec{k}} \cdot \sum_{\vec{k}'} f_{\vec{k}} f_{\vec{k}'} (n_{\vec{k}'} b_{\vec{k}} + b_{\vec{k}}^+ n_{\vec{k}'})) \quad (4)$$

Our trial function is simply the unrestricted linear combination $d|0\rangle + \sum_{\vec{k}} d_{\vec{k}}|k\rangle + \sum_{\vec{k}, \ell} d_{\vec{k}, \ell}|k, \ell\rangle$. We vary d , $d_{\vec{k}}$, and $d_{\vec{k}, \ell}$ to produce the variational minimum. For calculating the ground state, we set $p = 0$ in Eq. (4) and obtain variational equations which reduce to a one-dimensional integral equation. This equation, in turn, can be solved very readily by iteration. Some upper bounds to the ground state energy,[†] denoted ϵ_{gs} , are given in Table IV-1.

TABLE IV-1 UPPER BOUND FOR POLARON GROUND STATE ENERGY IN UNITS OF THE LO PHONON ENERGY							
α	0.5	1.0	1.5	2.0	3.0	4.0	5.0
ϵ_{gs}	-0.50400	-1.0160	-1.5361	-2.0640	-3.142	-4.247	-5.374

D. M. Larsen

[†] We are grateful to Susan Landon of Group 81 for assistance in the numerical computations.

Section IV

7. Upper Bounds on Number of Bound States for Nonlocal Potential

The number of bound states N of a particle in a nonlocal potential $W(\vec{r}, \vec{r}')$ has been considered. The Schrödinger equation is

$$(-\nabla^2 + \kappa^2) u(\vec{r}) + \int d\vec{r}' W(\vec{r}, \vec{r}') u(\vec{r}') = 0 \quad (5)$$

The inequality

$$N < - \int \frac{W(\vec{r}, \vec{r}')}{4\pi|\vec{r} - \vec{r}'|} d\vec{r} d\vec{r}' \quad (6)$$

has been derived by a generalization of a procedure used by Schwinger¹⁶ for a local potential. According to the derivation, this upper bound on N holds provided $W(\vec{r}, \vec{r}')$ is negative semi-definite. Other expressions for upper bounds have also been derived; the application of one of these expressions is described below. Both general and rotationally invariant potentials have been treated. Also, a criterion for demonstrating the nonexistence of a bound state has been found. Details of this work are available on request.

For a particle in a rotationally invariant nonlocal potential,

$$W(\vec{r}, \vec{r}') = (4\pi)^{-1} \sum_{\ell} (2\ell + 1) r^{-1} W_{\ell}(r, r') r'^{-1} P_{\ell}(\vec{r} \cdot \vec{r}' / rr') \quad (7)$$

where P_{ℓ} is the ℓ^{th} Legendre polynomial, the following class of bounds was derived

$$n_{\ell}(W_{\ell}, \kappa; p) < \int_0^{\infty} dr (g_{\ell} \tilde{u}_{\ell})^p(r, r, \kappa) \quad (8)$$

one bound for each ℓ, p value ($p = 1, 2, \dots$). In Eq. (8), $g_{\ell}(r, r', \kappa)$ is the Green's function used by Schwinger,¹⁶ and $\tilde{u}_{\ell}(r, r')$ — a comparison potential for $W_{\ell}(r, r')$ — is chosen to be positive semidefinite and such that $W_{\ell} + \tilde{u}_{\ell}$ is positive semidefinite; n_{ℓ} is an upper bound on the number of energy eigenstates with energy less than $-\kappa^2$.

As a test, Eq. (8) was applied to the potential

$$W(\vec{r}, \vec{r}') = \delta(r - r') V(\vec{r}) + U(\vec{r}, \vec{r}') \quad (9)$$

with local and nonlocal parts

$$V(\vec{r}) = -2(1 + r^{-1}) e^{-2r} \quad (10a)$$

$$U(\vec{r}, \vec{r}') = -2 e^{-r-r'}/\pi |\vec{r} - \vec{r}'| \quad (10b)$$

with components

$$V_{\ell}(r) = V(\vec{r}) \quad (11a)$$

$$U_{\ell}(r, r') = -8rr' e^{-r-r'} r_{<}^{\ell}/(2\ell + 1)r_{>}^{\ell+1} \quad (11b)$$

where $r_{<}$ ($r_{>}$) is the lesser (greater) of r and r' . This potential arose in an investigation of the minimum energy Slater determinant for the H^{-} ion.¹⁷ This potential occurs in one of the

Hartree-Fock¹⁸ (or Fock-Dirac-Slater) equations for the H^- ion when the two spins are parallel and the orbital for the other equation is a $1s$ hydrogen atom orbital. We know from other considerations¹⁹ that there are no bound states for the potential of Eq. (9).

We obtain the following results. We write Eq. (8) for $p = 1$ in the form

$$n_{\ell}(W_{\ell}, \kappa; 1) < I_{\ell}(\kappa) = I_{L,\ell}(\kappa) + I_{NL,\ell}(\kappa) \quad (12)$$

where the local and nonlocal parts are

$$I_{L,\ell}(\kappa) = - \int_0^{\infty} dr g_{\ell}(r, r, \kappa) V_0(r) \quad (13a)$$

$$I_{NL,\ell}(\kappa) = - \int_0^{\infty} \int_0^{\infty} dr dr' g_{\ell}(r, r', \kappa) U_{\ell}(r', r) \quad (13b)$$

Substituting from Eqs. (11a) and (11b), we find for $\kappa = 0$

$$I_{L,\ell}(0) = (3/2)/(2\ell + 1) \quad (14a)$$

$$I_{NL,\ell}(0) = \frac{16(2\ell + 2)}{(2\ell + 1)!} \sum_{k=2\ell+3}^{\infty} \frac{(k-2\ell)!}{k!} 2^{-(k+1-2\ell)} \quad (14b)$$

$I_{\ell}(0)$ decreases as ℓ increases. For $\ell = 0$, $I = 1.5 + 4 = 5.5$, so that there are at most five bound states. For $\ell = 1$, $I = 0.5 + 0.051 = 0.551$, so that there are no bound states for $\ell > 0$.

For $\ell = 0$, $\kappa > 0$

$$I_{L,0}(\kappa) = \frac{1}{2(\kappa + 1)} + \frac{1}{\kappa} \ln(1 + \kappa) \quad (15a)$$

$$I_{NL,0}(\kappa) = \frac{2(\kappa + 2)}{(\kappa + 1)^3} \quad (15b)$$

We note that $I_{NL,0}$ dominates in I_0 for $0 < \kappa < \kappa_c = 0.7444$; κ_c is defined by the equation $I_{L,0}(\kappa_c) = I_{NL,0}(\kappa_c)$. Also, if κ_n is the largest value of κ for which n bound states are allowed according to Eq. (12) [$I_0(\kappa_n) = n$], then $\kappa_5 = 0.0493$, $\kappa_4 = 0.1795$, $\kappa_3 = 0.3857$, $\kappa_2 = 0.7836$, and $\kappa_1 = 2.0323$.[†]

W. H. Kleiner
P. D. Fleming[‡]
T. A. Kaplan

B. MAGNETISM

1. Observation of Magneto-Elastic Coupling in Metallic Films

Spin wave resonance techniques have been used to study directly for the first time the magneto-elastic coupling of magnetic and elastic waves in magnetic metallic films. The effect

[†] After our investigation was finished, pertinent parts of a paper by Weinberg²⁰ came to our attention. This paper includes formulas from which all our results can be derived as special cases [see Weinberg's Eqs. (80) and (132)]. Moreover, Weinberg's derivation is less restrictive than ours in that the potential is not required to be negative semidefinite. Weinberg, however, does not elaborate the application of his results to nonlocal potentials, as we do.

[‡] Department of Physics and Department of Chemistry, Harvard University.

Section IV

has been recorded as the magnetic field deviation $\Delta\bar{H}$ of a given resonance peak from its normal quadratic dispersive behavior, in the absence of magneto-elastic coupling at a given microwave frequency ω .

The experimental parameters were carefully arranged so that the crossover region (that region where magnons and phonons of the same frequency have comparable wavevectors) could be adequately sampled by the allowed spin wave wavevectors. The range of ω was from 55.0 to 62.4 GHz. Film compositions ranged from the nonmagnetostrictive 81% Ni-19% Fe composition to 60% Ni-40% Fe. Film thicknesses were of the order of 6000 Å. Data were collected at room temperature and at liquid nitrogen temperature.

To explain the experimental results, a calculation was made which allowed for the solution of $\Delta\bar{H}$ in terms of appropriate parameters by combining a coupled system of equations consisting of the strain wave equations and an equation of motion for the magnetization.^{21,22} The system of coupled equations phenomenologically allowed both magnetic and elastic damping. Spin pinning and zero elastic stress boundary conditions were imposed, while the solutions for the transverse magnetization and for the elastic strain were obtained as sums of trigonometric functions. The pertinent dispersive result is

$$\Delta\bar{H} = \frac{b_2^2}{\rho M_S} \frac{(\omega^2 - c_t^2 k^2) k^2}{(\omega^2 - c_t^2 k^2)^2 + (2\omega/\tau_p)^2} \quad (16)$$

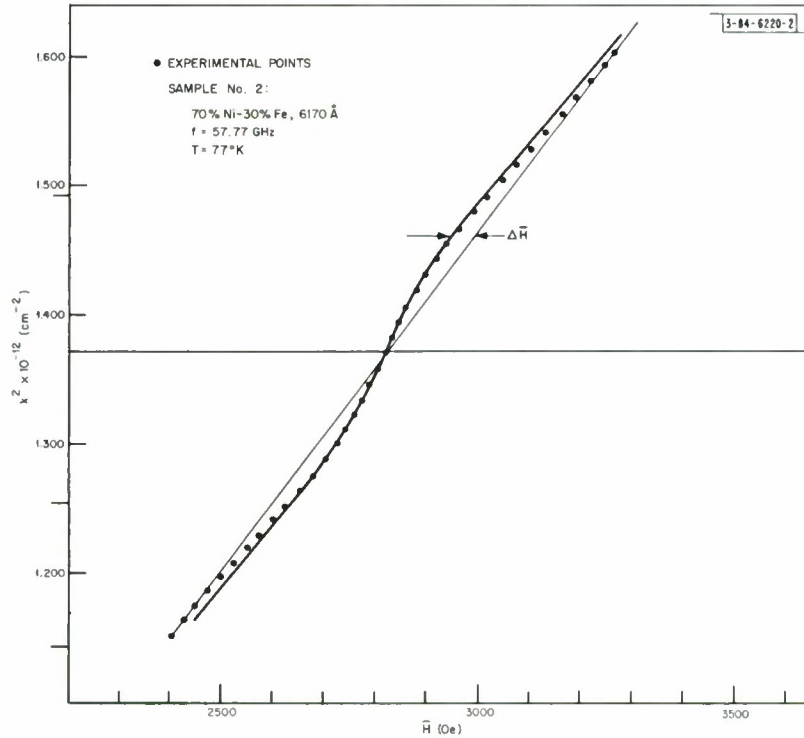


Fig. IV-10. Effect of magnon-phonon coupling in nickel-iron film. $\Delta\bar{H}$ is magnetic field deviation of given resonance peak from its normal quadratic dispersive behavior. \bar{H} is separation of given peak from uniform mode. In absence of coupling, $\bar{H} \propto k^2$.

where b_2 is the magneto-elastic coupling constant, c_t is the speed of transverse phonons of frequency ω in the film, ρ is the mass density, M_s is the saturation magnetization, and τ_p is the phonon relaxation time.

Figure IV-10 shows a fit of the above expression to the data for the 70%Ni-30%Fe film sample. Similar results were obtained for a 60%Ni-40%Fe sample while, for the nonmagnetostrictive sample, $\Delta\bar{H}$ was zero throughout the crossover region.

From the curve-fitting procedure, we determined that $c_t = 3.10 \times 10^5$ cm/sec, $|b_2| = 6.5 \times 10^7$ ergs/cm³, and $\tau_p = 0.9 \times 10^{-10}$ sec; these values are reasonable. It should be pointed out that the theoretical τ_p is that which would be obtained for a freely suspended film, whereas, in fact, the film is bonded to a glass substrate. Consequently, the measured τ_p may differ somewhat from the intrinsic relaxation time of the film material.

Calculations designed to explain the smooth transition of the resonances through the crossover region, to clarify the roles of the damping parameters, and to specify the effects of different combinations of possible boundary conditions are in progress.

R. Weber

2. Magnetic Resonance in Spinel Compound CoCr_2O_4

The microwave resonance data on CoCr_2O_4 giving the resonance field vs temperature for fixed frequencies are being analyzed on the basis of a modification of the molecular field model of Dwight and Menyuk.²³ At temperatures above the spiral spin ordering temperature (31°K), two modes are observed which we associate with a high-frequency exchange mode and a low-frequency uniform mode. The effective g-factor of the uniform mode drops sharply from 5.4 to 0.6 as the temperature is decreased from 85° to 31°K. This behavior, as well as the variation of frequency with temperature for both modes, requires the intrinsic g-factor of the cobalt cation to be of the order of 2.4. Modified molecular field calculations[†] are being made to determine the exchange parameters which give the best agreement between the DC magnetization and the microwave resonance data. Two resonance modes are observed below the spiral ordering temperature of 31°K. The interpretation of these modes is awaiting the results of the molecular field calculations presently under way.

J. J. Stickler
H. J. Zeiger

3. Magnetic Properties of MnAs

We have inaugurated a study of the effects of pressure on the magnetic properties of MnAs. This material is ferromagnetic at room temperature, and is known to undergo a first-order phase change from the hexagonal NiAs structure ($B8_1$) to the orthorhombic MnP structure ($B31$). This phase change, which occurs at about 318°K at atmospheric pressure, is accompanied by a discontinuous loss of ferromagnetism. The temperature at which the phase change occurs can be reduced by increasing the pressure, and Goodenough and Kafalas²⁴ have found that above 4500 atmos (4.5 kbars) the ferromagnetic $B8_1$ phase does not exist down to 4.2°K. Their determinations of the pressure and temperature dependence of the $B8_1 \leftrightarrow B31$ transitions were obtained on the basis of resistivity measurements. We have repeated their determination of the phase

[†] These calculations are based on a computer program kindly provided by K. Dwight.

Section IV

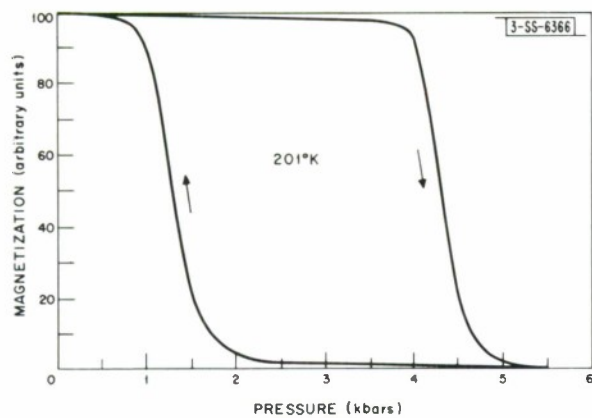


Fig. IV-11. Variation of magnetic moment of MnAs as function of applied hydrostatic pressure at 201°K.

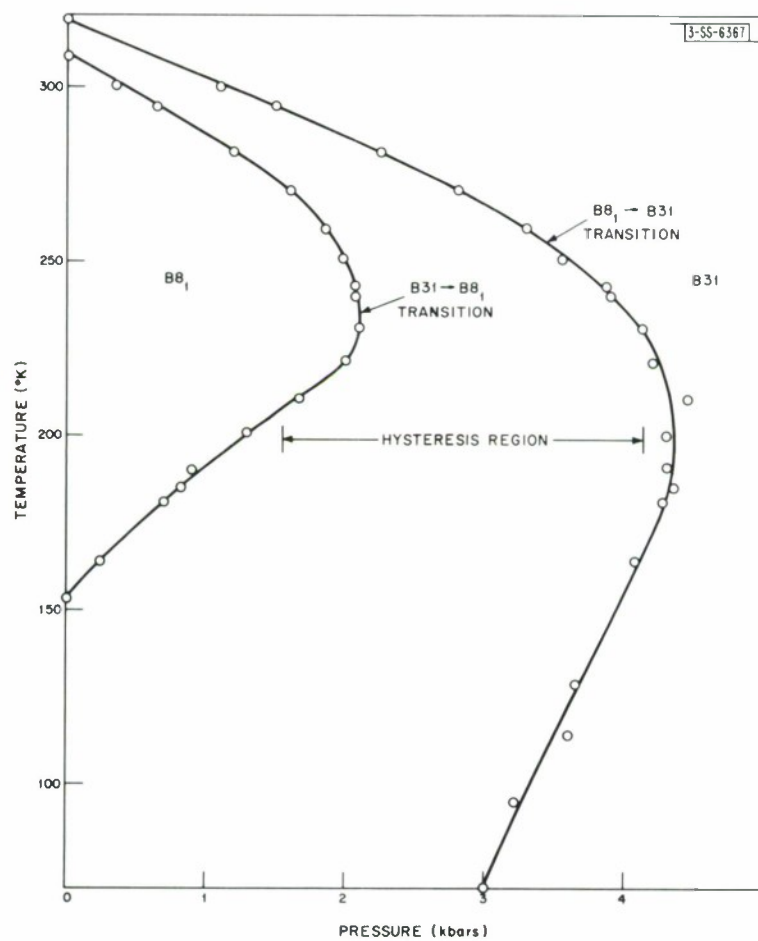


Fig. IV-12. Phase diagram of MnAs as function of pressure and temperature.

space, but by directly measuring the magnetic moment of a powder sample in a copper-beryllium vessel as a function of pressure. The vibrating-coil magnetometer is uniquely adapted to this type of measurement.

A typical curve of magnetic moment vs pressure at a fixed temperature in a field of 100 Oe is shown in Fig. IV-11. Defining the transition pressure $B_{8_1} \leftrightarrow B_{31}$ as that pressure at which 50 percent of the material is in the ferromagnetic state leads to the phase diagram shown in Fig. IV-12 which is similar to a diagram obtained by Goodenough and Kafalas.²⁴ The only significant difference is that we observe a distinct reduction in the $B_{8_1} \rightarrow B_{31}$ transition pressure with decreasing temperature below 200°K.

However, a larger number of points were taken in this measurement, enabling us to establish the curvature of $d\Theta/dT$, where Θ is the temperature of the $B_{8_1} \rightarrow B_{31}$ transition. Our results indicate a continuous change in $d\Theta/dT$ throughout the interval above 200°K. This disagrees with the conclusions of Grazhdankina and Bersenev,²⁵ who also studied this system above 200°K. They concluded that there were two distinct regions, above and below 270°K, with linear $d\Theta/dT$ values in each region but differing from each other by a factor of two. They felt this represented a new modification of MnAs. In part, they were led to this conclusion by noting that below 270°K they observed a reduction of the change in induction electromagnetic frequency on going through the transition. However, we find that the change in magnetic moment through the transition is essentially the same throughout the temperature interval investigated. This fact, coupled with the results shown in Fig. IV-12, lead us to conclude there is no transition at 270°K.

In agreement with Grazhdankina and Bersenev, we also have observed a magnetic transition at about 230°K at a pressure of 3.5 kbars. This transition becomes more pronounced at higher pressures, with a temperature dependence $dT_N/dP \approx 3^\circ/\text{kbar}$. Preliminary investigation of the region of phase space below this transition temperature indicates that the material is metamagnetic with a magnetic moment which is strongly dependent upon pressure. A thorough investigation of the magnetic properties in this region is contemplated as soon as a pressure vessel free of magnetic impurities is available.

N. Menyuk K. Dwight
J. A. Kafalas J. B. Goodenough

4. New Expansion for Classical Heisenberg Model and Its Similarity to $S = 1/2$ Ising Model

Following is an abstract of an article scheduled to appear in The Physical Review.

"The Heisenberg model susceptibility is expanded in the new expansion parameter $u \equiv \mathcal{L}(2J/kT)$ and a formal similarity with the $S = 1/2$ Ising model expansion is noted. General-lattice expressions for the new series are given through eighth order for close-packed and through ninth order for loose-packed lattices. The new Heisenberg model expansion is seen to permit comparison with Brown's recent work on the Bethe-Peierls-Weiss approximation, and to provide more reliable extrapolations for one-, two-, and three-dimensional lattices. In particular, evidence is presented that the critical exponent γ in the assumed form of the divergence of the susceptibility, $\chi \sim (T - T_c)^{-\gamma}$, has a value very close to 1.38 ($\approx 11/8$) for the fcc, bcc, and sc lattices."

H. E. Stanley

Section IV

5. Critical Properties of Vaks-Larkin Model for λ Transition in a Bose Fluid

Vaks and Larkin²⁶ have recently shown that near the λ point of a Bose fluid, the grand partition function is essentially equivalent to that of a lattice of isotropically interacting two-dimensional unit vectors (or classical spins) in zero external field. The Hamiltonian for this "planar Heisenberg model" of Vaks and Larkin is $\mathcal{H}^V = -2J \sum_{\langle f, g \rangle} (S_f^x S_g^x + S_f^y S_g^y)$, where $-2J$ is the energy of a nearest-neighbor pair of spins. Bowers and Joyce²⁷ have very recently calculated, for the f.c.c., b.c.c., and s.c. lattices, the high-temperature expansions for the reduced susceptibility

$$\bar{\chi}^V \equiv \chi^V / \chi_{\text{Curie}}^V = 1 + \sum_{n=1}^{\infty} a_n^V (J/kT)^n \quad (17)$$

and the specific heat

$$C^V = k \sum_{n=2}^{\infty} c_n^V (J/kT)^n \quad (18)$$

of the Vaks-Larkin model. We have obtained the corresponding expansions for general lattice structure, and have analyzed the series for specific one- and two-dimensional, as well as for three-dimensional, lattices. We also have re-expressed the susceptibility and internal energy series in terms of the new expansion parameter $w \equiv I_1(K)/I_0(K)$, where $K \equiv 2J/kT$ and $I_\nu(K)$ are the modified Bessel functions of the first kind. We find that this new expansion for the Vaks-Larkin model bears intriguing similarities to the corresponding expansions for the Ising model (one-dimensional spins) and the classical Heisenberg model (three-dimensional spins).

We find the specific heat series for the two-dimensional lattices to be so irregular that they cannot be readily used to estimate values of the critical temperatures $T_c^{(2)}$. However, the susceptibility series appear to diverge at nonzero $T_c^{(2)}$ for the plane triangular, square, and honeycomb lattices. This is particularly intriguing, since the indicated phase transition would have to be to a new type of low-temperature phase with no "infinite-range" order $M \propto \{\lim_{R \rightarrow \infty} \langle \vec{S}_0 \cdot \vec{S}_R \rangle_\beta\}^{1/2}$, yet with sufficient "long-range" order that $\chi \propto \sum_R \langle \vec{S}_0 \cdot \vec{S}_R \rangle_\beta$ diverges to infinity.

For the one-dimensional linear chain, both the susceptibility and specific heat series are too irregular to permit extrapolation to the known²⁶ result $T_c^{(1)} = 0$. However, we have obtained a much smoother series (and one which extrapolates directly to $T_c^{(1)} = 0$) by re-expanding the susceptibility in the new expansion parameter $w \equiv I_1(K)/I_0(K)$. The coefficients A_n^V in the new expansion

$$\bar{\chi}^V = 1 + \sum_{n=1}^{\infty} A_n^V w^n \quad (19)$$

are too lengthy to list here; however, they may be directly obtained from the (much less lengthy) expressions in Table IV-2 for a new set of coefficients D_n^V , defined by

$$\bar{\chi}^V \equiv (1 - \sigma w)^{-2} \left[1 - (\sigma - 1) w - \sigma w^2 + \sum_{n=3}^{\infty} D_n^V w^n \right] \quad (20)$$

on using the recursion relation $A_n^V = D_n^V + 2\sigma A_{n-1}^V - \sigma^2 A_{n-2}^V$. From Table IV-2, we see that for a "Bethe lattice" (a lattice with no polygons) $D_n^V = 0$ for $n \geq 3$ and Eq. (20) reduces to the result of the Bethe-Peierls approximation, $\bar{\chi}^V = (1 + w)/(1 - \sigma w)$.

TABLE IV-2
GENERAL-LATTICE EXPRESSIONS FOR THE D_n^V THROUGH ORDER $n = 8$
(Through Order $n = 9$ for the Subclass of Loose-Packed Lattices)

$$D_3^V = -6p_3$$

$$D_4^V = -8p_4 - 3p_3$$

$$D_5^V = -10p_5 - 4p_4 + 7.5p_3 + 6p_{5a}$$

$$D_6^V = -12p_6 - 5p_5 + 10p_4 + 13p_3 + 6[p_{6a} + p_{6b}] + 8p_{6c} + 38p_{5a}$$

$$D_7^V = -14p_7 - 6p_6 + 12.5p_5 + (7/3)p_4 + 5.25p_3 + 6[p_{7a} + p_{7b} + p_{7f}] \\ + 10p_{7c} + 8[p_{7d} + p_{7e}] + 66p_{7g} + 18p_{6a} + 41p_{6b} + 24p_{6c} + 12p_{6d} + (244/3)p_{5a}$$

$$D_8^V = -16p_8 - 7p_7 + 15p_6 + (35/12)p_5 + (44/3)p_4 - (343/24)p_3 + 6[p_{8a} + p_{8b} + p_{8c} + p_{8d}] \\ + 10[p_{8e} + p_{8f} + p_{8p}] + 8[p_{8g} + p_{8h} + p_{8i} + p_{8k}] + 12p_{8l} + 4p_{8q} + 72[p_{8r} + p_{8s}] \\ + 44[p_{7a} + p_{7b}] + 74p_{7c} + 24[p_{7d} + p_{7e}] + 18p_{7f} + 64p_{7g} + 10p_{7h} + 105p_{6a} \\ + (181/3)p_{6b} + 22p_{6c} - (37/3)p_{5a}$$

$$D_9^V = -8p_8 + 3.5p_6 + (26/3)p_4 + 6[p_{9k} + p_{9l}] + 8p_{9i} + 10p_{9m} \\ + 18p_{8c} + 24p_{8h} + 96p_{8r} + 8p_{8t} + (97/3)p_{7a} + 53p_{6a}$$

Section IV

By definition, the specific heat is the temperature derivative of the internal energy, which for a linear chain is $E^V = -2Jw$. Consequently, we have used our general-lattice expressions for the c_n^V of Eq. (18) to obtain the coefficients B_n^V in the new expansion

$$E^V = -(J/w) \sum_{n=2}^{\infty} B_n^V w^n ; \quad (21)$$

the general-lattice expressions for the B_n^V are given in Table IV-3.

TABLE IV-3 GENERAL-LATTICE EXPRESSIONS FOR THE B_n^V THROUGH ORDER $n = 9$ (Through Order $n = 10$ for the Subclass of Loose-Packed Lattices)	
$B_2^V = z$	
$B_3^V = 6p_3$	
$B_4^V = 8p_4$	
$B_5^V = 10p_5 - 9p_3$	
$B_6^V = 12p_6 - 12p_4 - 10.5p_3 - 18p_{5o}$	
$B_7^V = 14p_7 - 15p_5 + p_3 - 42p_{7g} - 21p_{6b} - 49p_{5a}$	
$B_8^V = 16p_8 - 18p_6 - (41/3)p_4 + (71/4)p_3 - 48[p_{8r} + p_{8s}] - 24[p_{7o} + p_{7b}]$ $- 56p_{7c} - 96p_{6d} - 28[3p_{6o} + p_{6b}] + (89/3)p_{5o}$	
$B_9^V = 18p_9 - 21p_7 + (5/3)p_5 + (485/24)p_3 - 54[p_{9e} + p_{9f} + p_{9h}] - 126p_{9g}$ $- 27[p_{8o} + p_{8b}] - 63[p_{8e} + p_{8p}] - 72[p_{8q} + p_{7h}] - 31.5p_{7b} + 40.5p_{7c}$ $- 63p_{7f} + 156p_{7g} + 0.75p_{6b} + 360p_{6d} + 180p_{5o}$	
$B_{10}^V = 20p_{10} - 24p_8 + 2p_6 + 25p_4 - 60[p_{10b} + p_{10c}] - 30p_{9k} - 70[p_{9m} + p_{8c}] - 80p_{8t}$ $+ 72p_{8r} - (107/3)p_{7o} + 136p_{6o}$	

The behavior of the new coefficients A_n^V and B_n^V is generally smoother than that of the coefficients a_n^V and c_n^V in the old expansions, thereby increasing the subjective reliability of extrapolations based thereon. Thus, for example, the critical indices suggested by the new series for three-dimensional lattices tend to support those proposed in Ref. 27. What is perhaps more important is that the Vaks-Larkin critical properties which we studied (T_c , γ , and α) appear to be bounded on one side by those predicted by Ising calculations, and on the other side by those predicted by the classical Heisenberg model. Also, the numerical values of the coefficients calculated (a_n^V , c_n^V , A_n^V , D_n^V , and B_n^V) are so bounded.

H. E. Stanley

C. LASER SCATTERING EXPERIMENTS AND NONLINEAR EFFECTS

1. Raman Scattering from Lowest Optical E-Vibration in α -Quartz

In order to interpret some stimulated Raman scattering results in quartz, we have calculated the dispersion curves in the vicinity of the lowest lying E-mode. The simplified equation

$$\epsilon = \frac{k^2}{\omega^2} = \epsilon_\infty + \sum_{i=1}^8 \frac{S_i \omega_i^2}{\omega_i^2 - \omega^2} \approx \epsilon'_\infty + \frac{S_1 \omega_T^2}{\omega_T^2 - \omega^2} \quad (22)$$

which neglects effects of anisotropy and damping, was used to plot the curves of Fig. IV-13. The effect of the seven higher E-modes is nearly constant over the range of frequencies computed, so it has been incorporated in ϵ'_∞ . The calculated IR strength in the upper transverse branch²⁸ is also shown. ϵ'_∞ and S_1 are taken from recent far-infrared data²⁹; this is to be contrasted to larger estimates^{30,31} of S_1 based on older IR measurements.³²

The resonant frequency and linewidth of this mode for various temperatures, shown in Table IV-4, have been measured by spontaneous Raman scattering from a He-Ne laser in a $z(y, z + y) \times$ geometry. The small frequency difference between the transverse and quasi-longitudinal branch could not be resolved.

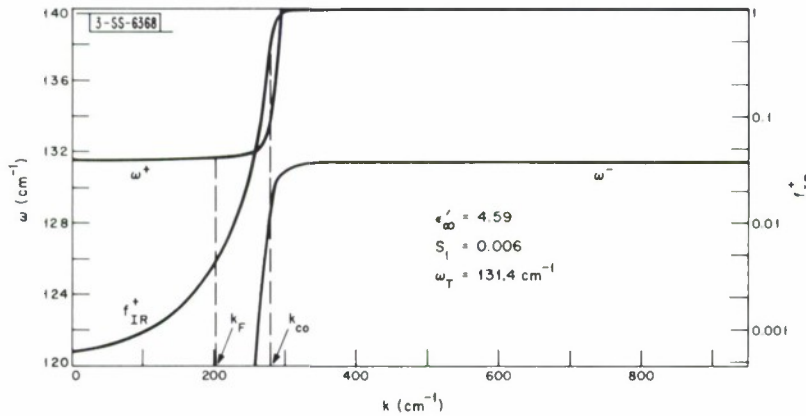


Fig. IV-13. Dispersion relations and infrared coupling fraction f_{IR}^+ for lowest optical E-mode in α -quartz. $\omega^+(k=0) - \omega_T = 0.09 \text{ cm}^{-1}$; $\omega^+(k=k_F) - \omega_T = 0.19 \text{ cm}^{-1}$; $\omega^+(k=k_{co}) - \omega^-(k=k_{co}) = 4.76 \text{ cm}^{-1}$.

Section IV

TABLE IV-4 FREQUENCY AND LINEWIDTH OF 128-cm ⁻¹ MODE			
T (°K ± 5°K)	300	85	15
ω_T (cm ⁻¹ ± 0.1 cm ⁻¹)	127.1	131.0	131.4
$\Delta\omega_T$ (cm ⁻¹ ± 0.3 cm ⁻¹)	3.7	< 0.5	< 0.5

Stimulated Raman emission has been achieved at low temperatures from the 128-cm⁻¹ mode by focusing a ruby laser at $f/3$ into a plane-parallel z-cut quartz crystal. The Raman emission is controlled by the quartz cavity³³ and occurs in a collimated beam of 2.8 ± 0.3 -mrad divergence along the normal to the quartz faces. This beam contains anti-Stokes radiation as well as several orders of Stokes of both the 128- and 466-cm⁻¹ modes. The total Raman power is ~1 MW, predominantly in the first Stokes of both modes. The Raman beam could be directed at any angle up to 0.2 rad (Dewar limitation) relative to the laser by tilting the quartz rod.

Anti-Stokes radiation accompanies the Stokes within the collimated beam for all tilt angles. Since the phase-matching angles for the anti-Stokes lines are small (<1 mrad for the 128-cm⁻¹ mode), this observation implies near-forward scattering using only those laser rays out of the focal cone almost collinear with the Stokes radiation. The Stokes shift, measured spectrographically, is 132 ± 1 cm⁻¹ independent of the angle of tilt. Presently, this resolution is inadequate to distinguish between exact forward scattering at $\omega^+(k = k_F)$, or exact backward scattering at ω_T as reflected into the forward direction by the cavity, as previously indicated.³⁴ However, in any case, no shift corresponding to small-angle scattering (~9 mrad) at the cross-over wavevector k_{co} occurs. Scattering from the LO branch is prohibited by symmetry³⁵ for the z-cut. The observed forward anti-Stokes may arise from stimulation of the $\omega^+(k_F)$ mode or may simply be driven parametrically by the laser and a forward Stokes wave which was originally generated backward. This latter process would be slightly nonresonant.

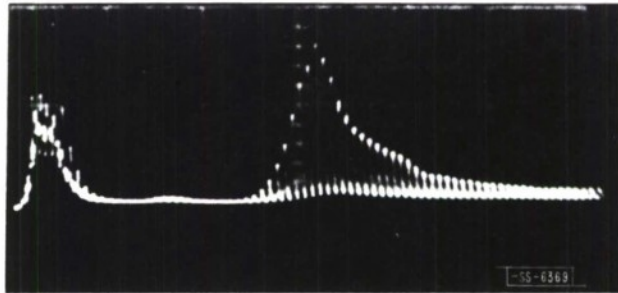
The fractional IR coupling of the E-mode for near-forward emission is not immeasurably small by itself. However, the relaxation rate as determined from the linewidth may be up to 100 times faster than the maximum generation rate as measured by the Stokes production. Additionally, anti-Stokes generation represents a phonon reabsorption process comparable in magnitude to phonon emission near the phase-matched angle. This would be particularly significant if the parametric, nonresonant process discussed above were dominant. To improve detectability of far-infrared radiation during the stimulated Raman process in quartz, we must optimize the experimental geometry to enhance the IR coupling.

P. E. Tannenwald N. D. Strahm
A. S. Pinc F. H. Perry

2. Mode Locking in Q-Switched Ruby Laser†

A new aspect to mode locking in a rotating-prism Q-switched ruby laser‡ has been recently observed. While spiking can be found in the output when the laser is only putting out one Q-switched pulse, the modulation is not regular unless the laser is close to threshold. However, when the laser is pumped hard enough to double pulse, the second pulse is quite different from the first in that it always exhibits a much more regular modulation (Fig. IV-14). Also, the extent of the modulation contained on the second pulse is not dependent on the amount the pumping exceeds the double-pulse threshold. The temporal spacing of the pulses is $\tau = 2L/c$, where L is the optical cavity length as in Ref. 36.

Fig. IV-14. Typical oscillogram demonstrating peculiar mode locking observed in ruby; this trace was taken with Tektranix 519 oscilloscope and ultra-fast planar diode. Peak power is ~ 50 MW/bax, and sweep rate is 50 nsec/cm.



This effect is believed to arise from the mode correlation which is established during the buildup of the first pulse via nonlinear population depletion and/or the rod acting as its own saturable absorber.³⁷ During the off time, between the first and second pulse, this mode correlation is retained; the buildup of the second pulse now tends to cause further mode correlation. Actually, as seen in Fig. IV-14, the second pulse can approach that of the dye mode locked laser in appearance. As a result, the second pulse may well contain spikes of narrower pulse width, and therefore higher peak power than the first; the spike pulse width is unresolved because of the response time of the scope plus photodiode (combined risetime 0.4 nsec).

While rod breakage is quite common in dye Q-switched lasers where care has not been taken to avoid mode locking, more recently a high breakage rate has been observed in rotating-prism Q-switched lasers in the double Brewster rod configuration operating close to the double-pulse threshold. If the above explanation is correct, then plano-Brewster rod configurations, which include a front reflector that is aligned with the plano cut, are a necessity in order to avoid the high breakage rate. To test this hypothesis and explanation, experiments on small-diameter ruby rods are now being carried out at the National Aeronautics and Space Administration Electronics Research Center in Cambridge, Massachusetts.

When a Nd glass rod is substituted for ruby, no tendency to mode lock is observed without the dye. This agrees with the predictions for the glass system.³⁷

R. L. Carman

† Experimental work was carried out using the facilities of the National Aeronautics and Space Administration Electronics Research Center in Cambridge, Massachusetts.

‡ Mode locking in a rotating-prism Q-switched ruby laser was reported previously.³⁶

Section IV

3. Thermal Defocusing of Light in Liquids

It is a well established fact that when a CW laser beam is passed through an absorbing liquid cell, the light will self-defocus with a time constant of the order of seconds. This effect³⁸ is due to the temperature dependence of the index of refraction, namely $n \sim n_0 - (\partial n / \partial T) \Delta T \equiv n_0 - \int n_2 \bar{E}^2 dt$. The latter part of the equality follows from the rise in temperature due to the linearly absorbed laser light. Just as a positive n_2 associated, for example, with the Kerr effect leads to self-focusing of light, a negative n_2 leads to self-defocusing, since a change in the index of refraction at the center of the beam with respect to the index at the extremities results in a change in the equiphase fronts in a manner identical to that of a lens. Because self-defocusing involves thermal properties, it is of course a relatively slow process, and therefore would be of little consequence in the case of ruby or Nd glass pulsed lasers, unless the absorption was relatively large.

The steady-state results have been derived and have been used to measure very low absorptions in liquids. The resultant effective focal length for a Gaussian beam is given by

$$F_{\infty} = - \frac{kn_0}{0.24\alpha \left| \frac{\partial n}{\partial T} \right| \ell} \left(\frac{\pi r_0^2}{p} \right) \equiv - \frac{\gamma}{\alpha \ell} \left(\frac{\pi r_0^2}{p} \right) \quad (23)$$

where k = thermal conductivity (cal/cm-sec °K), n_0 = index of refraction, α = optical absorption (cm⁻¹), r_0 = radius of CW laser beam (cm), p = CW laser power (W), ℓ = length of cell (cm), and $\gamma \sim 1$ in most liquids. For the case of $F \gg \ell$, the time dependence has been predicted³⁸ to be $F(t) = F_{\infty} (1 + t_c/2t)$ where $t_c = r_0^2 c_p / 4k$, c_p = specific heat (cal/g °K) and ρ = density (g/cm³).

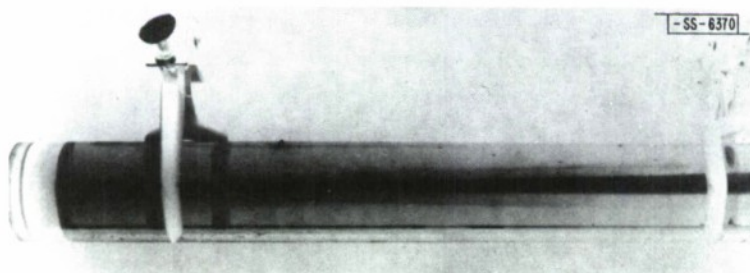


Fig. IV-15. Polaroid illustrating thermal self-defocusing of laser beam passing through 38-cm CCl₄ cell. Dye has been added to increase absorption at argon laser wavelengths.

There is a case which has received no attention experimentally, namely the thick-lens limit, or the case where $F \ll \ell$. Preliminary work has begun in investigating this limit; Fig. IV-15 is a Polaroid negative side view of a 38-cm cell containing CCl₄ and a dye to increase the absorption at the argon laser wavelengths, so that the thick-lens limit is reached. Quantitative studies of the time dependence of thermal defocusing in both limits are planned for the future.

R. L. Carman
P. L. Kelley

4. Infrared Radiation Effects on OH Maser Emission[†]

Infrared pumping which transfers population between the hyperfine states of the ground-state Λ -doublet has already been shown to result in maser emission of the satellite lines at 1612 and 1720 MHz (Ref. 39).

We have examined the possibility of observing maser emission from a Λ -doublet transition in an excited rotation or fine structure level in the ground electronic and vibrational states of OH. The population of excited levels, when not in thermodynamic equilibrium, will most likely be determined by trapped infrared resonance radiation and not by collisions. The two types of sources of far-infrared are: external sources due to a nearby star or nebula, and internal sources due to cascade following ultraviolet or chemical pumping and ultraviolet fluorescence, or due to hot protostar conditions. For cool clouds of OH, the hyperfine splitting of the rotational levels is taken into account in the infrared trapping problem. An integral equation of radiative transfer (similar to that of Sobolev⁴⁰) for a slab geometry and opposing radiation streams has been derived for interlocking hyperfine-split transitions, with complete frequency redistribution during backscattering. A simple but reasonably accurate solution to the integral equation has been obtained for the cases of arbitrary internal and external sources. The $\pi_{1/2}$ Λ -doublet seems to be strongly inverted, and the $\pi_{5/2}$ Λ -doublet anti-inverted, by ultraviolet or chemical pumping. The optical depths over which appreciable ultraviolet pumping and population inversion or anti-inversion of these states occurs greatly exceeds that for the ground state, since the ultraviolet flux integrated in frequency over the whole absorption line, and not just near line center as in selective absorption of a continuum pump, is effective in the generation of trapped infrared photons. The inversion of the excited Λ -doublet populations is proportional to the difference between the ultraviolet or chemical pumping rates of generating the infrared photons which connect to the upper and lower excited Λ -doublet states. While it is not likely that the maser emission is saturated, an observable signal in emission from the $\pi_{1/2}$ state, and absorption from the $\pi_{5/2}$ state, might be expected should the O5 ultraviolet pump star be a fraction of a light year away from the OH cloud.

M. M. Litvak

[†] This work was performed in collaboration with B. Zuckerman and D. F. Dickinson of the Harvard College Observatory and Smithsonian Observatory.

REFERENCES

1. Q.H.F. Vrehen, Phys. Rev. 145, 675 (1966); A. Frova, P. Handler, F.A. Germano, and D.E. Aspnes, Phys. Rev. 145, 575 (1966).
2. C.R. Pidgeon, S.H. Groves, and J. Feinleib, Solid State Commun. 5, 677 (1967).
3. V.I. Ivanov-Omskii, B.T. Kolomiets, V.K. Ogorodnikov, and K.P. Smekalova, Soviet Phys. – Semiconductors 1, 232 (1967) [translation from Fizika i Teknika Poluprovodnikov 1, 289 (1967)].
4. Z. Dziuba and T. Zakrzewski, Phys. Stat. Sol. 7, 1019 (1964).
5. C. Verie, Phys. Stat. Sol. 17, 889 (1966).
6. A.K. Ramdas and R. Aggarwal, Phys. Rev. 140, 1246 (1965).
7. W.E. Krag, W.H. Kleiner, H.J. Zeiger, and S. Fischler, Proceedings of the International Conference on the Physics of Semiconductors, Kyoto, Japan, 1966, in J. Phys. Soc. Japan 21S, 230 (1966), DDC 646490.
8. E.J. Johnson, Phys. Rev. Letters 19, 352 (1967), DDC 662293.
9. D.H. Dickey, E.J. Johnson, and D.M. Larsen, Phys. Rev. Letters 18, 599 (1967), DDC 658789.
10. D.H. Dickey and D.M. Larsen (to be published).
11. R. Bowers and Y. Yafet, Phys. Rev. 115, 1165 (1959).
12. C.R. Pidgeon and R.N. Brown, Phys. Rev. 146, 575 (1966).
13. G. Dresselhaus, Phys. Rev. 100, 580 (1955).
14. J.W. Hodby, J.A. Borders, F.C. Brown, and S. Foner, Phys. Rev. Letters (to be published).
15. D.M. Larsen, Phys. Rev. 144, 697 (1966), DDC 642204.
16. J. Schwinger, Proc. Natl. Acad. Sci. U.S. 47, 122 (1961).
17. Solid State Research Report, Lincoln Laboratory, M.I.T. (1966:3), p.42, DDC 641498, H-745.
18. A. Messiah, Quantum Mechanics II (Wiley, New York, 1963), p. 778.
19. T.A. Kaplan, P.D. Fleming, and W.H. Kleiner (unpublished).
20. S. Weinberg, Phys. Rev. 131, 440 (1963).
21. C. Kittel, Phys. Rev. 110, 836 (1958).
22. E. Schlömann, J. Appl. Phys. 31, 1647 (1960).
23. K. Dwight, N. Menyuk, and A. Wold, J. de Physique 25, 528 (1964).
24. J.B. Goodenough and J.A. Kafalas, Phys. Rev. 157, 389 (1967), DDC 661147.
25. N.P. Grazhdankina and Y.S. Bersenev, Soviet Phys. – JETP 24, 707 (1967).
26. V.G. Vaks and A.I. Larkin, Zhur. Eksp. i Teoret. Fiz. 49, 975 (1965) [translation: Soviet Phys. – JETP 22, 678 (1966)].
27. R.G. Bowers and G.S. Joyce, Phys. Rev. Letters 19, 630 (1967).
28. K. Huang, Proc. Roy. Soc. 208A, 352 (1951).
29. E.F. Russell and E.E. Bell, J. Opt. Soc. Am. 57, 341 (1967).
30. J.F. Scott and S.P.S. Porto, Phys. Rev. (to be published).
31. M.M. Elcombe, Proc. Phys. Soc. 91, 947 (1967).
32. R.B. Barnes, Phys. Rev. 39, 562 (1932).
33. P.E. Tannenwald, J. Appl. Phys. (to be published).
34. J.F. Scott, IEEE J. Quant. Electron. (to be published).

35. R. Loudon, *Advan. Phys.* 13, 423 (1964).
36. Solid State Research Report, Lincoln Laboratory, M.I.T. (1967:2), p. 47, DDC 656548.
37. H. Statz, G. DeMars, and C.L. Tang (to be published); C.L. Tang and H. Statz, *J. Appl. Phys.* 38, 323 (1967).
38. J.P. Gordon, *et al.*, *J. Appl. Phys.* 36, 3 (1965).
39. M.M. Litvak, A.L. McWhorter, M.L. Meeks, and H.J. Zeiger, *Astron. J.* 72, 812 (1967).
40. V.V. Sobolev, A Treatise on Radiative Transfer (Van Nostrand, Princeton, New Jersey, 1963), pp. 196 – 209.

DOCUMENT CONTROL DATA - R&D			
(Security classification of title, body of abstract and indexing annotation must be entered when the overall report is classified)			
1. ORIGINATING ACTIVITY (Corporate author) Lincoln Laboratory, M.I.T.		2a. REPORT SECURITY CLASSIFICATION Unclassified	
		2b. GROUP None	
3. REPORT TITLE Solid State Research			
4. DESCRIPTIVE NOTES (Type of report and inclusive dates) Quarterly Technical Summary - 1 August through 31 October 1967			
5. AUTHOR(S) (Last name, first name, initial) McWhorter, Alan L.			
6. REPORT DATE 15 November 1967		7a. TOTAL NO. OF PAGES 68	7b. NO. OF REFS 56
8a. CONTRACT OR GRANT NO. AF 19 (628)-5167		9a. ORIGINATOR'S REPORT NUMBER(S) Solid State Research (1967:4)	
b. PROJECT NO. 649L		9b. OTHER REPORT NO(S) (Any other numbers that may be assigned this report) ESD-TR-67-562	
c.			
d.			
10. AVAILABILITY/LIMITATION NOTICES This document has been approved for public release and sale; its distribution is unlimited.			
11. SUPPLEMENTARY NOTES None		12. SPONSORING MILITARY ACTIVITY Air Force Systems Command, USAF	
13. ABSTRACT This report covers in detail the solid state research work at Lincoln Laboratory for the period 1 August through 31 October 1967. The topics covered are Solid State Device Research, Optical Techniques and Devices, Materials Research, and Physics of Solids.			
14. KEY WORDS			
solid state devices	laser research	magnetism	electron beam pumping
optical techniques	crystal growth	Raman scattering	magnetoreflexion
and devices	band structure	magneto-elastic	magneto-optical
materials research	electroabsorption	magnetoabsorption	research
ion implantation	infrared	electroluminescence	phonons